NUMERICAL METHODS FOR SIMULATING DIFFUSION IN CELLULAR MEDIA

By

Trevor R.H. Sherk

Faculty of Science, University of Ontario Institute of Technology

December 14, 2011

A thesis submitted to the
University of Ontario Institute of Technology
in accordance with the requirements of the degree
of Master of Science in the Faculty of Science

Abstract

Diffusion imaging is a relatively recent branch of magnetic resonance imaging that produces images of human physiology through diffusion of water molecules within the body. One difficulty in calculating diffusion coefficients, particularly in the brain, is the multitude of natural barriers to water diffusion, such as cell membranes, myelin sheaths, and fiber tracts. These barriers mean that water diffusion is not a homogeneous random process. Due to the complexity of modeling these structures, a simplifying assumption made in some methods of data analysis is that there are no barriers to water diffusion. We develop tools to simulate the diffusion of water in an inhomogeneous medium, which may then be used to test the accuracy of this assumption. The inherent difficulty (and computational cost) of including barriers (e.g., cell membranes) can be lessened by employing the immersed boundary (IB) method to represent these structures without the need for complicated computational grids. The contribution of this thesis is the implementation and validation of an IB method that allows for diffusion across semi-permeable membranes. The method is tested for a square interface aligned with the computational grid by comparing it to a second numerical scheme that uses standard finite differences. We also calculate the rate of convergence for the IB method to assess the numerical accuracy. To demonstrate the flexibility of the IB method to simulate diffusion with any interface shape, we also present simulations for irregular interfaces.

Acknowledgements

Many thanks to my supervisor, Dr. Greg Lewis, for being a great help and source of encouragement during the course of my undergraduate and graduate studies. I could not have asked for a better supervisor for this project.

I would also like to thank my family who have encouraged me along the way to stay focused and finish well. My friends at Gospel for Asia, where I am currently working, have also been a tremendous help this past year. Their support and understanding has helped me to keep working hard and successfully finish. I also give thanks to God - my rock, my strength, and the One upon whom I put my trust (Psalm 18:2).

To the staff and faculty at UOIT who have provided me with an excellent atmosphere for learning and growing as an individual, thank you. It has been a very enjoyable part of my life which I will take with me as I pursue future studies and careers.

Author's Declaration

I declare that this work was carried out in accordance with the regulations of the University of Ontario Institute of Technology. The work is original except where indicated by special reference in the text and no part of this document has been submitted for any other degree. Any views expressed in the dissertation are those of the author and in no way represent those of the University of Ontario Institute of Technology. This document has not been presented to any other University for examination either in Canada or overseas.

Trevor R.H. Sherk

Date: December 14, 2011

Contents

List of Figures

List of Tables

Chapter 1

Introduction

1.1 Background

Diffusion MRI is a relatively recent branch of magnetic resonance imaging (MRI) that has been used to produce detailed maps of human physiology as well as various porous structures. Diffusion MRI [34] attempts to infer structural information about the material being imaged by interpreting MRI signals based on simplifying models of *diffusion*, the displacement of particles undergoing random (Brownian) motion, self-propelled by thermal energy [30].

In a broader sense, MRI is a well-known, non-invasive imaging technique for visualizing internal structures with a high degree of detail. It is capable of providing good contrast between different types of soft tissues in the body and is widely used to indirectly image the human brain, the heart, muscles, and even to spot tumours.

Diffusion did not play an important role in early MRI development and study. The first experiments to combine diffusion-weighted magnetic resonance measurement with MRI were not published until 1984 [27]. However, since the 1990s, developing and improving diffusion imaging techniques has become a research area of great interest due to established success in clinical neurodiagnostics [15] and projected benefits. In addition, ongoing research into diffusion MRI techniques is helping to provide a greater understanding of diffusion in living systems. Complex data acquisition schemes (e.g. echo planar imaging [8, 24]) are also being developed that may enhance and improve the feasability of these methods.

This thesis presents numerical tools that may be used to study diffusion and assess the validity of diffusion models used by many diffusion MRI schemes. Specifically, the contribution of this thesis is the implementation and validation of an immersed boundary method for the simulation of cellular diffusion. The first chapter of this work provides a discussion of current diffusion MRI schemes. The second chapter briefly discusses diffusion in membrane-separated systems, including those found in brain tissue. A simplified model of diffusion in membrane-based systems is then presented. In Chapter 3, we discuss the immersed boundary (IB) method and apply it to the governing equations of our diffusion model. In Chapter 4, we present the results from our simulations using the IB method to verify its applicability to such biological problems. The strengths and weaknesses of our proposed numerical method will be reviewed in the fifth chapter as well as suggestions for future work. We begin with a brief overview of diffusion MRI and the motivation for developing the tools presented in this thesis.

1.2 Diffusion Magnetic Resonance Imaging Techniques

Current and future applications of diffusion MRI offer the potential to provide in vivo detail of the anatomy and connectivity of the brain that normal MRI cannot. The type of structural information that may be obtained indirectly from diffusion MRI depends on the imaging scheme used. These range from the simplest - the mapping of apparent diffusion coefficients - to the more complex, such as diffusion tensor imaging, q-ball imaging, diffusion spectrum imaging, and tractography [15]. We begin our discussion of these various imaging techniques with an integral part of all diffusion MRI schemes - the probability density function.

1.2.1 Probability density function p

In statistical terms, the erratic motion of diffusing particles can be described by the displacement distribution which indicates the proportion of particles that will move a given distance, in a given direction, at a given time. The "diffusion coefficient", D, is a constant that determines some averaged measure of displacement and is related to the mean square displacement of a given particle.

Diffusion MRI attempts to approximate the probability density function p of particle displacements over a fixed time based on MR signals and either some assumption of the displacement distribution (e.g., Gaussian distribution for free water molecules), or a large sample of diffusion-weighted images. Because the microstructure of a material determines the mobility of particles within, studying the features of p can allow indirect imaging of microstructures.

In biomedical diffusion MRI, water molecules are the particles of primary interest since water is a major constituent of biological tissue. However, determining the form of the displacement distribution is very difficult, particularly in the brain, due to the multitude of natural barriers to water diffusion, such as cell membranes, myelin sheaths, and fiber tracts. These barriers mean that water diffusion is not a homogeneous random process. Specifically, in a homogeneous medium, if you draw the displacement distribution for one location in the domain, it would be the same under translation to another location in the domain. A homogeneous domain also implies that the displacement distributions will follow a multivariate Gaussian (bell-shaped) function, corresponding to either isotropic diffusion (equal diffusion coefficient in all directions) or anisotropic diffusion. For this reason, it is helpful to think of the diffusion coefficient as a variance of the Gaussian distribution.

The heterogeneity of biological tissue implies that the distributions are not Gaussian. Indeed, the distribution's form depends on the internal structures themselves. Due to the complexity of modeling these structures, a simplifying assumption made in some methods of data analysis is that there are no barriers to water diffusion.

1.2.2 Diffusion-weighted and Diffusion-tensor Imaging

To interpret and extract data from the MR signal data, the most commonly used diffusion imaging techniques use this hypothesis for the displacement distribution of water molecules diffusing over a fixed time. Diffusion-weighted imaging and diffusion tensor imaging assume that diffusion follows a multivariate Gaussian function. This is an accurate description for the diffusion of water in a homogeneous medium. However, biological tissue is highly heterogeneous, such as the white matter tissue in the brain. For example, neuronal tissue (axons) are expected to produce a preferred direction of diffusion as water molecules will move more freely (i.e., faster) on average along the axon membranes, and much slower in a perpendicular direction due to the cell membrane restriction [15]. For such heterogeneous media, the assumption of a Gaussian diffusion distribution is clearly wrong.

The attraction to these imaging schemes is their simplicity, low hardware requirements and short acquisition times compared to more complex methods such as diffusion spectrum imaging. Diffusion-weighted imaging (DWI) uses just one image for each voxel (three-dimensional volume, typically 1mm^3 in size). A diffusion-weighted image is the unprocessed result of a single pulsed gradient spin-echo sequence in one gradient direction, with one gradient strength. This scheme is used in more complex techniques to reconstruct the probability density function p, such as in diffusion spectrum imaging. A routine clinical application for DWI is in investigating strokes [27]. When cells die, they expand, causing the extracellular space to decrease around them, restricting the movement of water molecules. This can be detected through DWI as an increase in the MR signal intensity, allowing the radiologist to determine areas affected by acute stroke.

Because of the ability to provide information regarding the anisotropic nature of diffusion rather than the isotropy of DWI, diffusion tensor imaging (DTI) has a host of potential applications, such as fibre-tracking or 'tractography' to indirectly image neural tracts in the brain and study brain connectivity [5]. DTI has already been used to image fiber tracts in white matter, which, if accurate, could potentially provide lifesaving information for neurosurgery. While standard MRI is able to obtain structural information of a patient's brain to spot tumours, for example, it cannot assess the orientation and intersection of axonal fibers. To carefully treat brain cancer, the neurosurgeon needs to know how to access the tumour, and what regions she can cut into without causing further damage [12]. Such information, if it could be obtained reliably in the future from diffusion MRI, would be of obvious interest. Other clinical applications for DWI and DTI are in studying white-matter diseases such as epilepsy, multiple sclerosis and dementia [5]. Apart from studying the brain, diffusion imaging schemes are also used to investigate the microstructure of a variety of porous materials including muscle tissue (e.g. in the heart), cartilage, plant tissue, and porous rock [5].

1.2.3 Advanced Methods of Data Analysis

In addition, it should be noted that not all diffusion imaging schemes are based on the Gaussian distribution hypothesis for diffusion. There are more complex diffusion imaging techniques in use that are either based on a different hypothesis, or no hypothesis at all.

Q-ball imaging is one technique that, as in DTI, is based on a hypothesis about the shape of the diffusion probability density function p. One shape that is sometimes assumed for p is that of a pincusion [15]. In this case, it is assumed that the compartments inside an imaging voxel can be represented by straight and thin pipes with impermeable walls. Water molecules inside the pipes are therefore assumed to diffuse uniformly parallel to the pipes but cannot diffuse across the impermeable walls. However, further studies are required to validate q-ball imaging reconstruction techniques as an accurate scheme for all regions of the brain, although it is considered to provide realistic depictions of complex fiber architecture [15]. Another drawback for q-ball imaging is that it is impractical for use in a clinical setting due to hardware requirements being high and long image acquisition times.

Perhaps the most complex diffusion imaging scheme, also with considerable acquisition time, is diffusion spectrum imaging (DSI). In contrast to the diffusion tensor model, DSI is not based on a particular shape or hypothesis for p. Instead, it relies on hundreds of diffusion weighted images, with applications of frequency-encoding gradients that vary in strength and direction. This process is used to sample a large proportion of "q-space", the space corresponding to diffusion gradients with a specific direction and strength. If a sufficiently dense sample of q-space is provided by DSI, the displacement distribution, or diffusion probability density function p, can be derived with the use of a Fourier transform. Established practice suggests 515 diffusion-weighted images for a particular diffusion time interval to provide good quality data [15]. However, with advances in hardware and imaging techniques, and recent experience, some suggest that p can be derived with fewer sampling points [15]. This leads to shorter acquisition times, and makes DSI more feasible for clinical studies.

1.3 Motivation for New Imaging Schemes

Ideally, we would like an imaging scheme that does not require long acquisition times (such as DWI or DTI), but also provides microstructure information not based on a hypothesis for the displacement distribution (such as DSI). One such solution would be to remove the hypothesis from DWI and DTI that diffusion follows a Gaussian distribution. To replace the Gaussian distribution with a different shape, we would first need to have an understanding of how a variety of microstructures (e.g. axons) affect the shape of p. DWI and DTI schemes could then be modified to take into account numerous shapes for p when interpreting MR signals.

It is difficult to predict the shapes of the displacement distributions p in the presence of water restriction, such as in the case with semipermeable membranes. However, through the use of advanced numerical techniques, simulations of diffusion in heterogeneous media can be performed and corresponding displacement distributions calculated. Using the standard definitions for diffusion due to thermal energy and imposing restrictions to diffusive movement, such as a simple membrane representation, it is possible to set up such simulations.

In our study, we develop numerical tools to simulate diffusion in heterogeneous media such as brain tissue, with permeable membranes. While this could potentially be used to test the hypothesis used in DWI and DTI of a Gaussian distribution, other applications include modeling diffusion in contrast-enhanced perfusion magnetic resonance imaging, and aiding the development of new drugs. Based on an understanding of how a drug will diffuse, it could be designed to target specific parts of the body.

The inherent difficulty (and computational cost) of representing barriers to diffusion (e.g., cell membranes) in a simulation can be significantly lessened by employing an immersed boundary method (IBM). The IBM allows for representing various structures without the need for complicated computational grids. It is an efficient numerical scheme that is becoming very popular for simulating fluid-structure problems. To our knowledge, the IBM has not been applied to simulating diffusion in heterogeneous matter involving discontinuous diffusion coefficients and semipermeable membranes.

Chapter 2

Mathematical Models of Diffusion in Cellular Media

Diffusion is a process that plays a very important role in the everyday function of living organisms. Biological systems involving membrane-based separations rely heavily on the diffusion properties of cellular membranes, such as the ability for water molecules to pass in and out of cells [30]. Even the molecular mechanics controlling the organization of macromolecules are known to include elements of diffusive processes at several stages [38].

It is possible that information about cellular microstructures may be obtained by studying the diffusion of particles as they pass through and go around the microstructures. In particular, biological diffusion magnetic resonance imaging (MRI) tracks the diffusion of water molecules since MRI is best suited for these molecules specifically. To represent diffusion and interpret MR signals, a displacement distribution p is often used. One difficulty, however, is in predicting the shape of p in heterogeneous material.

As previously mentioned, simplifying models for the displacement distribution (such as the Gaussian function) are often used to reconstruct images of microstructures. This is particularly problematic for diffusion in the brain, which is known to be highly heterogeneous. To provide more accurate information from diffusion imaging, the displacement distribution p for such matter must be better understood.

To determine the most relevant features of p, one must first understand the basics of diffusion and how structures such as cell membranes can affect diffusion. We will focus on structures found in brain tissue, as this is an area of considerable interest both in research development of diffusion MRI, and also in clinical use.

2.1 Diffusion in Cellular Media

Diffusion is the random migration of molecules or small particles, self-propelled by thermal energy [30]. The thermal energy of fluids such as water at typical (room or body) temperatures can be associated with this constant random motion of the molecules. Over time, the molecule or particle will become randomly displaced by some distance x (without the influence of external forces), and will on average tend towards areas with fewer elements of its own type due to frequent molecular collisions.

In biological systems, the motion of molecules passing between the inside and outside of a cell can essentially be described as a random walk [13]. This may seem counter-intuitive as one expects a more orderly and deterministic manner of motion for a system to remain stable. However, through ongoing studies of diffusion, there is much evidence that this principle regularly governs diffusion in living systems.

The first person known to report observations of the random walk in nature was the botanist Robert Brown, in 1828 [38]. His study of pollen particles from various plants placed in water discovered an irregular “swarming” motion. The random molecular collisions responsible for the observed motion is today called Brownian motion, and technically concerns the motion of a colloidal particle in a liquid [38]. An analogy between the colloidal particles in a liquid and (clusters of) molecules can be made for biological systems because, similarly, the size of surrounding solvent particles is much smaller than the molecules [38]. Due to this, the random walk picture is regularly used to describe diffusion in living systems.

Living matter is structured and ordered by various biological components, such as cell membranes (soft interfaces), fibers, and scaffolding structures. These structures can range in scale from nanometers to the size of whole cells and organisms. Typically, however, the length scales are in the 1-1000 nm range. For such a small scale, over time scales relevant in biology, the process of diffusion in cellular media, although random in nature, can actually serve a deterministic purpose in supporting the functioning of the cell [38].

We expect that due to the structure of living matter, diffusion of particles often occurs in highly heterogeneous matter. Such anisotropic conditions may result in behaviour that is markedly different than expected for isotropic conditions. There have been many studies and models written for diffusion in isotropic conditions, but relatively few for anisotropic diffusion. It is not clear how well results obtained using the assumption of isotropy relate to biological systems because of the presence of structures such as membranes and fibres, which violate the assumption of isotropy. More research is required to better understand the process of diffusion in heterogeneous matter as well as to predict the shape of the displacement distribution.

2.2 Biological Membrane Systems

All cells are surrounded by cell or plasma membranes which offer protection and serve numerous functions (e.g., facilitating ion conduction, cell-to-cell chemical and electrical signaling, and controlling movement of particles in and out of cells). These membranes can be thought of as thin elastic sheets, with a total thickness of a few nanometers typically [38]. A soap bubble is a simple analogy to biological membranes that surround our cells. They are fragile and flexible, and can change properties with the influence of external forces, such as heat. However, the complexity of biological membranes and the significant role that they play is far greater than that of soap bubbles.

One popular model used to illustrate and explain the properties of cell membranes is called the “Fluid Mosaic Model.” This description captures the fluid-like nature in which lipid molecules pass one another relatively easily, the heterogeneity due to distinct small-scale phases and internal structures, and the various cellular compartments with their specific functions [38]. The chemical composition and structure of membranes is such that they allow most lipids to pass through, and selectively restrict the passage of ions, sugars, and amino acids [1].

Even though diffusion is often assumed to take place under isotropic conditions, this assumption is especially poor for regions in which membrane-based separations are present. Numerous experiments have revealed that tagged molecules can become confined to a region for some time, or that the mean square displacement will sometimes exhibit unexpected behaviour [38].

Due to the heterogeneity and complexity of membranes, there are various obstacles to the passage of large molecules and particles through the membrane. For short diffusion times, the presence of such barriers to diffusion can clearly have a great effect on the rate of diffusion. When short times are being studied (such as with diffusion MRI), it is therefore crucial to accurately describe the effect of the membranes on diffusion. However, if the long-term behaviour is of primary interest, the effect of such membranes can be greatly diminished or even become negligible [38].

Thanks to advances based on new experimental techniques and theoretical modeling, a better understanding of membranes and their importance has emerged [38]. We will develop a simple brain tissue model that can represent either isotropic or anisotropic conditions as a numerical tool in further exploring biomedical diffusion problems in the presence of semipermeable membranes.

2.3 Diffusion in the Brain

One feature of the human brain's architecture is its complex network of grey matter areas connected by millions of white matter fibers. Grey matter consists mostly of nerve cell bodies (neurons) and glial cells, but also contains dendrites and synapses [2]. The grey matter region of the brain is responsible for processing information which is then transmitted through neuronal axons (in white matter). Neurons (“nerve cells”) are complex brain cells with specialized membranous structures, and numerous supporting elements, such as embedded and peripheral proteins and ion channels [3]. Glial cells are nerve cells that do not carry electro-chemical signals. Their role is mainly supportive, helping the brain digest parts of dead neurons, supporting healthy neurons, and more. White matter is composed of those neuronal axons, which connect nerve cell bodies to one another in various grey matter areas. The axons carry nerve impulses between neurons.

Each type of brain cell is unique not only in its function, but also in size, shape, and composition. Furthermore, the differences in cell structures and orientation can lead to significant changes in the shape of the displacement distribution. In the context of biomedical diffusion MRI, these differences are of great importance. Through calculating and imaging the average displacements of hydrogen atoms in water molecules, one can infer structures based on the rate of diffusion in a region. For this reason, we are most interested in simulating the movement of water molecules inside the brain. To illustrate how diffusion can vary depending on tissue type and configuration, we consider a few possible scenarios that occur in the brain.

To describe the diffusion of water molecules in the brain, one could draw contours of the expected probability density function p for a particular tissue and configuration. This function describes the probability that a particle will move in a given direction due to random diffusion. As mentioned already, diffusion in grey matter can differ greatly qualitatively and quantitatively from diffusion in white matter.

In regions of the brain that are mostly fluid-filled, such as in ventricles (which contain mostly cerebrospinal fluid), particle displacements are equally likely in any direction because microstructural barriers to water movement are relatively few [5]. The function p in this case is isotropic.

Conversely, in the dense tissue of grey matter there are several barriers to water mobility such as cell walls and membranous structures. In the case where such barriers are not aligned in any particular orientation, the function p remains isotropic. However, the shape of p will be narrower since the average length of displacement is smaller than without the barriers.

In white matter, neuronal axons are oriented parallel to each other with a greater consistency than that of cell walls in grey matter. As displacements parallel to the fibre axis are larger on average than in directions perpendicular to the fibre axis, the function p is anisotropic. White matter also contains more complex microstructures with fibres crossing each other, sometimes orthogonally. In this case, p is anisotropic with ridges in the direction of each fibre [5]. Other configurations of structures may occur in the brain, with different shapes of p, but these are the most common examples.

Having summarized some of the various types and configurations of brain tissue, we briefly discuss a model of diffusion in cellular media that can be applied to brain tissue configurations and parameters. Due to the complexity of the brain, defining a model for diffusion of water molecules in the brain is a challenging task. Furthermore, the range of tissue types in the brain, and their varying arrangements, sizes, shapes and functions means that such a model must be flexible, although it will nevertheless be a broad simplification of actual diffusion. It should, however, capture the key characteristics of diffusion in both isotropic and anisotropic conditions.

2.4 Simple Brain Tissue Model

We wish to develop a model that represents diffusion of particles across semipermeable membranes. Using such a model, simulations could be run with varying permeability, shapes of membranes, and other cellular characteristics. Through such simulations, we wish to have the ability to demonstrate the influence on average rate of displacement caused by the presence of semipermeable membranes. As such, the effect of isotropic and anisotropic conditions on the displacement distribution could be investigated. This would be a valuable tool that could be used to better understand the influence of cellular membranes on diffusion, and one that could potentially be applied to various medical applications that involve diffusion in cellular media.

2.4.1 Restricted Diffusion in Cellular Media

The model we develop is for the restricted diffusion of particles, e.g., water molecules, in living tissue with cellular boundaries. The particular application is to the diffusion of water molecules inside brain tissue (e.g., grey or white matter), with molecules that may move around and across brain cell membranes.

It is well-understood that water molecules are allowed to move through cell membranes of living tissue [18], albeit at a much slower rate than in a free (homogeneous) medium. In this heterogeneous domain, we wish to model the diffusion that would occur with given initial concentrations, brain cell sizes and configurations, and diffusion times.

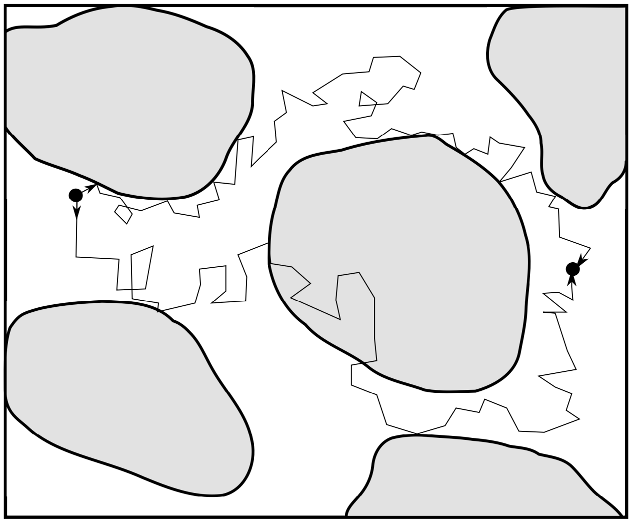

Figure 2.1: Cartoon of cellular water diffusion; shaded regions represent cell bodies and the solid interfaces surrounding them represent the cellular membranes. The random movement of particles in the intra- and extracellular space is depicted by two alternate diffusion pathways. In one pathway, the particle diffuses across the center cell's membrane, whereas in the second pathway, the particle goes around. Reproduced following Figure 1 from [21].

We consider a configuration of intracellular and extracellular space separated by semipermeable interfaces, such as that in Figure 2.1. The intracellular and extracellular spaces have characteristic diffusion coefficients, D_I and D_O, respectively. Thus, due to the complexity of structures inside the cell, the average rate of diffusion inside the cell should be much smaller than the rate outside the cell, meaning that D_I is less than D_O.

2.4.2 Model Assumptions

To simplify our model, we assume homogeneity both inside and outside the cell, while the overall heterogeneity of brain tissue is modelled by separating the extracellular and intracellular fluid with a semipermeable interface of zero thickness. This of course is not accurate because of the presence of larger molecules and structures inside the membrane, such as the nucleus. However, we assume that these smaller scale inhomogeneities are less important than the overall cell tissue heterogeneity.

The justification for such a model is that we can still represent the overall effect of the cellular membranes as well as restricted diffusion inside the cell by selecting appropriate permeability coefficients for the membrane, as well as characteristic diffusion coefficients for the average rate of displacement of particles inside and outside the cell.

To study the displacement distribution for diffusion in cellular media, we assume that the most important factors are the shape of membranes, their permeabilities, and the relative diffusion coefficients inside and outside the cell. The shape of the boundary can be changed easily using the immersed boundary method, which we discuss in Chapter 3. In addition, the diffusion coefficients and membrane permeability are also parameters that may be changed to model various tissue configurations.

2.4.3 Typical Brain Tissue Parameters

The diffusion coefficients and permeability found in brain tissue vary based on numerous factors, and can be difficult to calculate experimentally. However, for the purpose of our model, we consider the following parameters to be typical for brain tissue, and are based on the work Latour et al. [21] (see also Szafer et al. [32] for similar parameters):

$$\begin{aligned} D_I &= 1.56 \times 10^{-5} \ \ \mathrm{cm}^2/\mathrm{s}, & D_O &= 2.12 \times 10^{-5} \ \ \mathrm{cm}^2/\mathrm{s}, \\ P &= 0.01 \ \ \mathrm{cm/s}, & a &= 2 \ \mu\mathrm{m}, \end{aligned}$$

where D_I and D_O are the intracellular and extracellular diffusion coefficients, respectively, P is the permeability coefficient (the rate of permeation of particles through the interface Γ, with dimensions of conductivity), and a is the cell radius of a spherical cell.

The inequality between diffusion coefficients D_I and D_O is due to the greater number of microstructures inside the cell that impede water diffusion than those outside the cell.

The diffusion times used in our simulations are typically 1ms or less. Note that for such short diffusion times, the effects of cell membrane and anisotropy can be studied well. A good example is a human axon, with a typical diameter of $0.8 - 2$ µm [4]. For a particle within an axon and a diffusion coefficient of $D = 1.56 \times 10^{-5}\ \ \mathrm{cm}^2/\mathrm{s}$, the particle could travel a distance of 1.2 µm in 1ms. Therefore, the diffusing particle will potentially reach the cell walls multiple times, and either diffuse across the membrane or become reflected. Alternatively, for a cell nucleus with a diameter of 4 µm, the particle would not likely reach the cell membrane in this time. Axons can be modelled well with the IB method by considering long, parallel membranes. This is left for future work, but is worthwhile in investigating anisotropic diffusion found in the brain (e.g. in grey matter). Similarly, the research by Szafer et al. [32] (through Monte Carlo simulations) offers excellent insight into a broad range of diffusion times for similar cellular diffusion problems. The relationships between apparent diffusion coefficient and such factors as the membrane permeability and cell size are also presented.

Based on the theoretical principles presented above for diffusion in cellular media, we now present the governing equations for our mathematical model.

2.4.4 Governing Equations

The canonical equation to describe free diffusion of molecules or small particles is

$$c_t = \nabla \cdot \left(D \nabla c \right), \tag{2.4.1}$$

where c is the concentration of particles and D is the diffusion coefficient. This governing equation is derived from two laws proposed by Adolf Fick. The first law,

$$\mathbf{J} = -D \nabla c, \tag{2.4.2}$$

provides the equation for the diffusive flux, $\mathbf{J}$, as a linear relation to the concentration gradient ∇c, with D as the proportionality coefficient.

As mentioned, diffusion is the random movement of molecules or small particles due to thermal energy. Diffusion is also loosely defined as the sporadic tendency of systems to equalize concentration in the absence of impeding external forces [30]. The flux equation therefore reflects the property that atoms, molecules, or any particle will migrate (through diffusional processes) in the direction where fewer elements of its own kind are located (from high concentration to low concentration). An additional law relating diffusive flux to concentration is Fick's second law,

$$\frac{\partial}{\partial t}c + \nabla \cdot \mathbf{J} = 0, \tag{2.4.3}$$

which captures mathematically the principle of conservation of mass, i.e., that particles cannot be created or destroyed, as expected for a normal diffusion process. Substituting (2.4.2) into (2.4.3) yields the diffusion equation (2.4.1).

To include the inhibiting effect of the interface (cell membrane) on the free diffusion of particles, a *flux law* is needed at the interface Γ. The magnitude of net flux across the interface may be modelled as

$$J = -P\ A\ \left(c_2 - c_1\right), \tag{2.4.4}$$

(in three-dimensions) where P is the membrane permeability, A is the surface area of the membrane, and $c_2 - c_1$ is the difference in concentration across the membrane for flow from c_1 to c_2 (e.g., flow from intracellular concentration to extracellular concentration). That is, we assume that the flux across the membrane is directly proportional to the jump in concentration across the membrane.

We consider a general form of (2.4.4) which includes the possibility of relating flux to a nonlinear change of concentration across the membrane. We write the flux law at the interface Γ in 2D as:

$$D\nabla c = P\left[g(c)\right]_{\Gamma}\mathbf{n}, \tag{2.4.5}$$

where $[\,\cdot\,]_\Gamma$ denotes the jump across the interface, $g(c)$ is a function of concentration, and $\mathbf{n}$ is the unit normal vector of the interface. The flux through the interface Γ described by (2.4.5) will have a magnitude given by the membrane permeability times the jump in concentration at the interface, as given by $g(c)$ (see Figure 2.2). We assume that flux is zero in the tangential direction, a simplification that is a good approximation when the driving force of particle motion is the concentration gradient of the system, not the fluid velocity. In this case, flux in the tangential direction would be negligible in comparison to flux in the normal direction, e.g., through cell membrane pores, the main means of particle transport.

The inclusion of a general $g(c)$ allows for a variety of linear or nonlinear laws depending on the problem being studied and the particular application. For our model, we assume a linear function of concentration, $g(c) = c$.

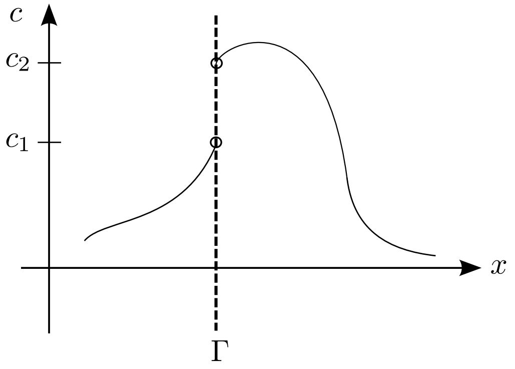

Figure 2.2: Discontinuous concentration in 1D with jump in concentration given by $[g(c)]_\Gamma$.

Summarizing our brain tissue model, the governing equation for diffusion in the bulk region is given by

$$c_t = \nabla \cdot (D \nabla c)\,, \tag{2.4.6}$$

and the flux law at the interface is

$$D \nabla c = P\,[c]_\Gamma\,\mathbf{n}. \tag{2.4.7}$$

Here we assume homogeneous diffusion inside and outside the cells, and model the overall heterogeneity of the brain tissue with the flux law (2.4.7) at an interface Γ of zero thickness. The diffusion coefficient $D = D(\mathbf{x})$, permeability P, and shape of Γ may be varied to simulate diffusion in various brain tissue configurations, e.g., for glial cells and neuronal cells in grey and white matter.

In Chapter 3, we present our numerical methods for producing simulations. The immersed boundary (IB) method is discussed, and governing equations are reformulated under this framework to demonstrate the applicability, challenges, and benefits of using this powerful numerical technique for such fluid-structure problems.

Chapter 3

Immersed Boundary Method for Cellular Diffusion

Having presented our simple model for diffusion of particles in cellular media with semipermeable membranes, we propose an efficient numerical method to perform computational simulations. We use the immersed boundary (IB) method to easily impose the effect of embedded interfaces (membranes) of any shape and size without setting up complex computational grids.

We begin with an overview of IB methods and how they are used. We then apply the IB method framework to our governing equations to derive equations valid on the entire computational domain. Using the concept of flux as an additional variable, we have a system of coupled equations which can model diffusion in the presence of any arbitrary interface configuration. To run simulations, we solve the resulting equations numerically by applying the Crank-Nicolson numerical scheme. This produces a linear system of equations representing the evolution in time of particle concentrations for each point in the computational grid. We are then able to run our simulations for a variety of cellular parameters and configurations, the results of which are presented in Chapter 4.

3.1 The Immersed Boundary Method

In 1972, Charles S. Peskin developed a method for simulating the pumping motion of the human heart and associated fluid dynamics of the blood flow [28]. His approach employed a single Cartesian grid which did not conform to the heart geometry, and featured an entirely new method for expressing the effect of an *immersed boundary* on fluid flow. This boundary, or interface may be, for example, a membrane immersed in a fluid, or an interface between two different fluids.

Numerous variants and refinements of his immersed boundary (IB) method have since been developed, and are generally classified as such if they simulate viscous flows with embedded interfaces on grids not conforming to the shape of the immersed objects. Due to its simplicity, the IB method has become one of the main numerical techniques for scientific computation of fluid-structure interaction problems, including those involving moving interfaces [18, 25, 29]. A similar class of methods, often termed "Cartesian grid methods", has also been developed for simulating inviscid flows [9, 10, 40]. These too have been extended to simulate unsteady viscous flows [37, 39], with capabilities similar to those of IB methods [25].

To simulate flow past an immersed solid body (see Figure 3.1*a*), the conventional approach employs structured or unstructured grids conforming to the shape of the object. The generation of the grid proceeds in two general steps. First, generate a surface grid covering the boundary Γ_b. A grid in the fluid volume Ω_f is then generated with the surface grid as its boundary condition.

If a conventional finite difference method on a structured grid is used for the the representation of governing equations, special care is needed because the immersed boundary (hereafter termed 'interface'), in general, does not coincide with the grid. The finite difference form of the governing equations must be transformed to a curvilinear coordinate system aligned with the grid lines to make the discretisation of the transformed equations somewhat simpler. If a finite volume method is used instead, the integral form of the governing equations is discretised and the shape of the interface may be incorporated directly into the discretisation.

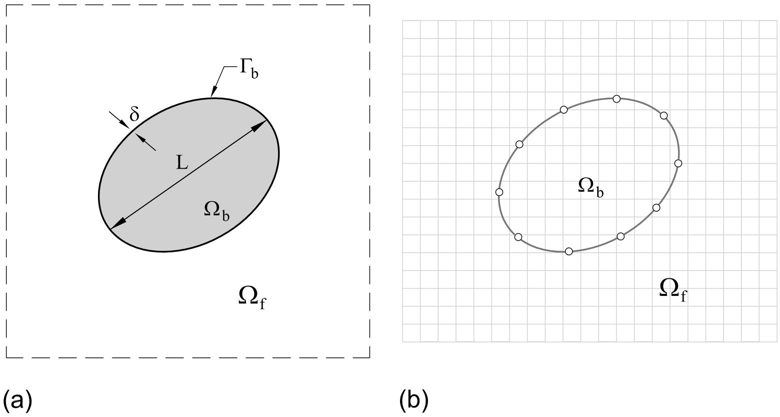

Figure 3.1: (a) An immersed body around which a flow is to be simulated. The body has volume Ω_b, boundary Γ_b, length scale L, and a boundary layer of thickness δ. (b) An immersed boundary in a Cartesian grid on which the governing equations are discretised. Reproduced following Figure 1 of [25].

When using unstructured grids, both finite volume and finite element methods may be used. Grid transformations are not needed in either approach, allowing the interface to be represented somewhat more easily. However, for both structured and unstructured grids, the amount of work required to account for arbitrarily shaped interfaces, especially ones lacking symmetry, is quite significant [25]. For flows with moving boundaries, the generation of body-conformal grids requires the use of a dynamic mesh, which, for the finite element method, can be very inefficient. The solution must then be projected onto the new grid at every time step. As such, the computational cost and accuracy of the solution procedure will be severely affected for large motions [25]. Including body motion using the IB method, however, is simpler due to the use of a fixed (in time) Cartesian grid.

In Figure 3.1b, we consider a nonbody-conformal Cartesian grid that is used in the immersed boundary method. The interface is represented through means such as a surface grid Ω_b as before (e.g., a set of Lagrangian points). However, instead of building an unstructured grid around the interface, a structured, Cartesian grid Ω_f is generated *independent* of the surface grid that cuts through Ω_f.

The immersed boundary method requires a modification of the governing equations to enable imposing boundary conditions on the interface. The modifications to the governing equations will depend on the problem being solved, and can take a variety of forms. This step distinguishes IB methods from one another and is the most significant aspect of developing an IB method algorithm. See [25] for an excellent discussion on the many approaches used in imposing boundary conditions on immersed boundaries.

After the appropriate modification has been made, the governing equations are then discretised using a numerical scheme (e.g., finite difference, finite element, or finite volume) without any coordinate transformations required. This greatly reduces the per-grid-point operation count, and the simplicity is one of the benefits of the IB method. In this way, the IB method has become an attractive approach for simulating fluid flow problems with moving boundaries.

Before discussing the specifics of our numerical methods, it is useful to compare the advantages and disadvantages of the IB method as it compares to other techniques. The primary advantage of the IB method is that the task of grid generation is greatly simplified [25]. Conversely, generating body-conformal structured or unstructured grids can be very cumbersome. For instance, with body-conformal grids, we often seek a grid providing relatively high resolution around the boundaries, while attempting to minimize the number of total grid points. This can be quite challenging for increasingly complex geometries. Furthermore, structured body-conformal grids may suffer from grid smoothness deterioration between interfaces of subdomains of varying grid sizes. With the IB approach of employing a non body-conformal Cartesian grid, algorithm and grid complexity are not significantly affected by the geometric complexity of an immersed boundary.

The advantage of body-conformal grids, however, is that they tend to allow for better control of the grid resolution in the vicinity of the body [25]. In fluid-structure problems, this has implications for the increase in grid size required with increasing Reynolds number (a dimensionless constant used in fluid mechanics problems to distinguish between flow regimes and quantify the relative importance of viscous and inertial forces in the equations of motion). As the Reynolds number increases, the number of grid points for an accurate approximation of flow around the boundary layer increases. For a Cartesian grid, the increase of the required grid points is faster than for a corresponding body-conformal grid. This does not necessarily imply a corresponding increase in computational cost, however, as a substantial fraction of the grid points may be inside the solid body where fluid flow equations need not be solved [25].

Another disadvantage of IB methods is that they are known to require small time steps to maintain stability and accuracy when solved with explicit methods. Some implicit and approximately implicit methods have been proposed in the literature to remove the severe stability constraint, but are typically too computationally expensive, with little improvement in the rate of convergence [17]. Due to these drawbacks, practical computations using the IB method typically use an explicit discretisation, despite the time step requirements. However, one promising numerical method is a semi-implicit scheme (i.e., based on an implicit scheme, but is effectively explicit) that was proposed by Hou and Shi [17] as an IB method for solving the Navier-Stokes equations. They are able to significantly improve the accuracy of the numerical solution, with a computational cost comparable to that of an explicit scheme. Such approaches, with advanced algorithms to improve the accuracy near the interface are more complex and therefore less easily implemented. However, there is much to be gained by such methods, and they are certainly a good option for those desiring highly accurate quantitative information in the entire domain.

We use the Crank-Nicolson method in the discretisation of the governing equations. This scheme (which is implicit in time) is a popular choice because it has been shown to be unconditionally stable, and is simple to implement. However, this comes at an expense to the accuracy of the solution, and is therefore a tradeoff between simplicity and accuracy. We will discuss the advantages and disadvantages of such a scheme further in Chapter 4 along with numerical simulations for 1D and 2D problems. In Section 3.2 we apply the IB method framework to reformulate the governing equations, and then use the Crank-Nicolson method in Section 3.3 to discretise the new governing equations.

3.2 An Immersed Boundary Method for Cellular Media

Since the development of Peskin's original IB method, there have been a number of non-biological fluid-structure applications proposed, and the interest continues to grow. Suspension flows [31], parachute dynamics [20], and multimaterial simulations [35] are a few recent examples of such applications. Biological and multiphase flows, however, continue to be the most common use of the IB method.

In a recent paper by Huang et al., an IB method was proposed for the restricted diffusion of a fluid through permeable interfaces. Examples of such flows include heat transfer processes restricted at contact boundaries [16], and diffusion of water and oxygen molecules restricted by cell membranes in biological tissues [19]. The approach used in the IB formulation is the continuous forcing process (see [25]), where a set of governing equations valid on the entire domain are formulated to impose the effect of the interface on fluid motion. The coupled equations are valid in both the bulk region Ω_f and the interface Ω_b (see Fig. 3.1).

The key idea behind Huang et al.'s approach is to use flux $\mathbf{f}$ as an additional variable in the formulation of model equations for concentration c. The approach of using flux as an unknown function for diffusion problems, however, is not new; in fact it also appears in mixed finite element methods (see, for example [7, 11, 6]). Using c and $\mathbf{f}$, Huang et. al. formulate a set of equations which are valid in the entire domain Ω, including on the interface Γ. The delta function proposed by Peskin is used in the flux and concentration equations to impose the effect of the interface on the diffusion of particles. This approach, however, leads to a smoothing of the desired discontinuity in concentration at the interface. Some have proposed advanced methods to more accurately capture the discontinuity at such interfaces. Leveque et al. [23] and Layton [22] propose some numerical techniques, which also address the short time step restraint.

However, these methods, and many others, have not yet (to our knowledge) been applied to the diffusion equation with discontinuous diffusion coefficients and semipermeable interfaces. This particular diffusion problem is the main interest in our study, and simulations of diffusion of particles in cellular media. In our numerical method, we discretise the model equations proposed by Huang et al. [18]. They provide an elegant and powerful means of simulating diffusion for arbitrarily shaped interfaces, with relative ease.

3.2.1 Reformulating the Governing Equations under the IB Method

At the interface Γ, there will be a discontinuity in concentration c, as expressed implicitly in the interface flux law (3.2.1),

$$D\nabla c = P\left[c\right]_\Gamma \mathbf{n}, \tag{3.2.1}$$

where D is the diffusion coefficient, P is the permeability, $[\,\cdot\,]_\Gamma$ denotes the jump across the interface, and $\mathbf{n}$ is the unit normal vector of the interface. We assume that c is smooth everywhere except at the interface, and define

$$c = c^s + \left[c\right]_\Gamma H\left(\mathbf{x} - \mathbf{x}_\Gamma\right), \tag{3.2.2}$$

where $[c]$ is the jump in concentration across the interface Γ and H is the Heaviside step function. The discrete form of H is zero on one side of the interface and one on the other side. This gives us discontinuous concentration at Γ because

$$\lim_{x\to x_\Gamma^-} c = c^s, \quad \text{and} \quad \lim_{x\to x_\Gamma^+} c = c^s + \left[c\right]_\Gamma.$$

Now we take the gradient of both sides of (3.2.2):

$$\begin{aligned}\nabla c &= \nabla c^s + \nabla\left(\left[c\right]_\Gamma H\left(\mathbf{x} - \mathbf{x}_\Gamma\right)\right), \\ &= \nabla c^s + \mathbf{n}\int_\Gamma \left[c\right]_\Gamma \delta(\mathbf{x} - \mathbf{x}_\Gamma)\mathbf{dx}_\Gamma, \end{aligned} \tag{3.2.3}$$

where we have used the following relationship between the Heaviside step function and the delta function:

$$\nabla H(\mathbf{x}-\mathbf{x}_\Gamma) = \mathbf{n}\int_\Gamma \delta(\mathbf{x}-\mathbf{x}_\Gamma)\mathbf{dx}_\Gamma. \tag{3.2.4}$$

Rearranging the interface flux law (3.2.1), we have

$$\mathbf{f}\cdot\mathbf{n} = -D\nabla c\cdot\mathbf{n} = -P\left[g(c)\right]_\Gamma .$$

If we use the following approximation,

$$\left[g(c)\right]_\Gamma = g'(c_{\text{avg}})\left[c\right]_\Gamma , \tag{3.2.5}$$

where c_{avg} is the average of c_I and c_E (intracellular and extracellular concentration, respectively), then we have

$$\begin{aligned} \frac{-\mathbf{f}\cdot\mathbf{n}}{P} &= \left[g(c_{\text{avg}})\right]_\Gamma , \\ &= g'(c_{\text{avg}})\left[c\right]_\Gamma , \\ \Rightarrow \frac{-\mathbf{f}\cdot\mathbf{n}}{Pg'(c_{\text{avg}})} &= \left[c\right]_\Gamma . \end{aligned} \tag{3.2.6}$$

For our model, we let $g(c) = c$, which means that $g'(c) = 1$. This term, which is used in the following equations, and not $g(c)$, is scalar and does not depend on concentration c. Therefore, we can replace c_{avg} by c for simplicity. For $g(c)$ different from c, we would have to denote which c we choose for the approximation in (3.2.5). Combining (3.2.6) with (3.2.3) we have

$$\begin{aligned} \nabla c &= \nabla c^s + \mathbf{n}\int_\Gamma \left[c\right]_\Gamma \delta(\mathbf{x}-\mathbf{x}_\Gamma)\mathbf{dx}_\Gamma, \\ &= \nabla c^s + \mathbf{n}\int_\Gamma \frac{-\mathbf{f}\cdot\mathbf{n}}{Pg'(c)}\delta(\mathbf{x}-\mathbf{x}_\Gamma)\mathbf{dx}_\Gamma, \\ &= \nabla c^s - \int_\Gamma \frac{\mathbf{f}}{Pg'(c)}\delta(\mathbf{x}-\mathbf{x}_\Gamma)\mathbf{dx}_\Gamma, \end{aligned} \tag{3.2.7}$$

where we again use the assumption that flux $\mathbf{f}$ is zero along Γ.

Now we multiply by the diffusion coefficient D. At this point we will assume that D

is continuous everywhere, whereas in a real-life problem involving cellular membranes, this is not the case. Typically, the intracellular and extracellular diffusion coefficients are not the same, so there should be a discontinuity in D across the interface. We will approximate the jump in D by a function $D(\mathbf{x})$ that changes quickly from one side of the boundary to the other. Numerically, this is achieved by setting $D = D_I$ inside the interface, $D = D_O$ outside, and $D = \frac{1}{2}(D_I + D_O)$ on the interface.

Multiplying (3.2.7) by the diffusion coefficient, we have:

$$D\nabla c + \int_\Gamma \frac{D\mathbf{f}}{Pg'(c)}\delta(\mathbf{x} - \mathbf{x}_\Gamma)\mathbf{dx}_\Gamma = D\nabla c^s.$$

Next we take the divergence of both sides:

$$\nabla \cdot \left(D\nabla c + \int_\Gamma \frac{D\mathbf{f}}{Pg'(c)}\delta(\mathbf{x} - \mathbf{x}_\Gamma)\mathbf{dx}_\Gamma\right) = \nabla \cdot \left(D\nabla c^s\right).$$

Because flux is continuous everywhere (due to conservation of mass), $[c]_\Gamma$ does not contribute to the flux $D\nabla c^s$, thus

$$\nabla \cdot \left(D\nabla c^s\right) = -\nabla \cdot \mathbf{f} = c_t.$$

We now have the governing equation for concentration, valid on the entire domain Ω:

$$c_t = \nabla \cdot \left(D\nabla c + \int_\Gamma \frac{D\mathbf{f}}{Pg'(c)}\delta(\mathbf{x} - \mathbf{x}_\Gamma)\mathbf{dx}_\Gamma\right). \tag{3.2.8}$$

We also seek an equation to compute flux $\mathbf{f}$ on Ω. We begin by finding an equation for $\mathbf{f}$ in the subdomain Ω/Γ. Consider the following identity:

$$\nabla\left(g'(c)c_t\right) = g'(c)\left(\nabla c\right)_t + g''(c)c_t\nabla c. \tag{3.2.9}$$

In the subdomain Ω/Γ, $c_t = \nabla \cdot (D\nabla c)$. Substituting this into (3.2.9), we have

$$\nabla\left(g'(c)\nabla \cdot (D\nabla c)\right) = g'(c)\left(\nabla c\right)_t + g''(c)\nabla \cdot \left(D\nabla c\right)\nabla c.$$

Now we multiply both sides by D and replace $D\nabla c$ by $-\mathbf{f}$:

$$-D\nabla\left(g'(c)\nabla\cdot\mathbf{f}\right) \;=\; -g'(c)\mathbf{f}_t + g''(c)\mathbf{f}\nabla\cdot\mathbf{f}.$$

Rearranging, we have

$$g'(c)\mathbf{f}_t = g''(c)\mathbf{f}\nabla\cdot\mathbf{f} + D\nabla\left(g'(c)\nabla\cdot\mathbf{f}\right). \tag{3.2.10}$$

Additionally, by using the interface flux law (3.2.1), we can obtain an equation valid for Γ:

$$\begin{aligned} -\mathbf{f} &= P\left[g(c)\right]_\Gamma \mathbf{n}, \\ -\mathbf{f}\cdot\mathbf{n} &= P\left[g(c)\right]_\Gamma . \end{aligned}$$

Now we take the time derivative:

$$\begin{aligned} -\mathbf{f}_t\cdot\mathbf{n} &= P\left[g'(c)\frac{\partial c}{\partial t}\right]_\Gamma, \\ &= P\left[g'(c)\nabla\cdot\left(D\nabla c\right)\right]_\Gamma, \\ &= P\left[g'(c)\nabla\cdot\left(-\mathbf{f}\right)\right]_\Gamma, \\ \Rightarrow \mathbf{f}_t\cdot\mathbf{n} &= P\left[g'(c)\nabla\cdot\left(\mathbf{f}\right)\right]_\Gamma . \end{aligned} \tag{3.2.11}$$

Combining (3.2.10) and the interface flux law (3.2.1) yields an equation in $\mathbf{f}$ on the entire domain Ω that we use to solve for flux:

$$\mathbf{f}_t\left(g'(c) + \int_\Gamma \frac{D}{P}\delta(\mathbf{x}-\mathbf{x}_\Gamma)d\mathbf{x}_\Gamma\right) = g''(c)\mathbf{f}\nabla\cdot\mathbf{f} + D\nabla(g'(c)\nabla\cdot\mathbf{f}). \tag{3.2.12}$$

To verify that (3.2.12) is valid for all of Ω, we can consider the subdomain $\mathbf{x}\in\Omega/\Gamma$ and interface Γ separately. In $\mathbf{x}\in\Omega/\Gamma$, it is straightforward to see that (3.2.12) yields (3.2.10). On the interface Γ, we can obtain the time derivative of the interface flux law (3.2.1), given by (3.2.11), by integrating (3.2.12) across the interface Γ. Because we use $g(c) = c$ in our model, to simplify the presentation, we will substitute this into

(3.2.12) before integrating.

Choosing $g(c) = c$ also means that $g'(c) = 1$, and $g''(c) = 0$. Substituting these into (3.2.12) yields:

$$\mathbf{f}_t \left(1 + \int_\Gamma \frac{D}{P}\delta(\mathbf{x} - \mathbf{x}_\Gamma) d\mathbf{x}_\Gamma\right) = D\nabla(\nabla \cdot \mathbf{f}). \qquad (3.2.13)$$

Now we integrate both sides across Γ in the normal direction as follows:

$$\lim_{\epsilon\to 0}\int_{\gamma+\epsilon}^{\gamma-\epsilon} \mathbf{f}_t \left(1 + \int_\Gamma \frac{D}{P}\delta(\mathbf{x} - \mathbf{x}_\Gamma) d\mathbf{x}_\Gamma\right) \cdot \mathbf{n}\; dn = \lim_{\epsilon\to 0}\int_{\gamma+\epsilon}^{\gamma-\epsilon} D\nabla(\nabla \cdot \mathbf{f}) \cdot \mathbf{n}\; dn, \quad (3.2.14)$$

where $\mathbf{n}$ is the unit normal vector to the interface (pointing outward as shown in Fig. 3.2). To integrate the left-hand-side of (3.2.12), we expand and integrate each part separately.

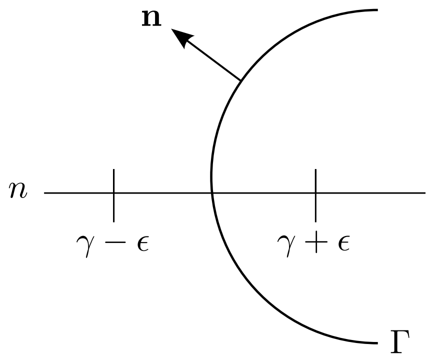

Figure 3.2: To verify that (3.2.12) is valid on the interface, we integrate across Γ in the normal direction, $\mathbf{n}$. The vector $\mathbf{n}$ is the unit normal vector of the interface.

First, because $\mathbf{f}$ is continuous across the interface Γ, we have:

$$\begin{aligned}
\lim_{\epsilon\to 0}\int_{\gamma+\epsilon}^{\gamma-\epsilon} \mathbf{f}_t \cdot \mathbf{n}\; dn &= \lim_{\epsilon\to 0} [\mathrm{F_t}(\gamma - \epsilon) - \mathrm{F_t}(\gamma + \epsilon)] \cdot \mathbf{n}, \\
&= \mathrm{F_t}(\gamma) - \mathrm{F_t}(\gamma), \\
&= 0,
\end{aligned}$$

where we have used the Fundamental Theorem of Calculus and let F_t be the antiderivative of f_t on $[\gamma - \epsilon, \gamma + \epsilon]$. Secondly, we have:

$$\begin{aligned} \lim_{\epsilon \to 0} \int_{\gamma+\epsilon}^{\gamma-\epsilon} \mathbf{f}_t \left(\int_\Gamma \frac{D}{P} \delta(\mathbf{x} - \mathbf{x}_\Gamma) d\mathbf{x}_\Gamma \right) \cdot \mathbf{n} \; dn, &= \lim_{\epsilon \to 0} \frac{D}{P} \int_{\gamma+\epsilon}^{\gamma-\epsilon} \int_\Gamma \mathbf{f}_t \delta(\mathbf{x} - \mathbf{x}_\Gamma) d\mathbf{x}_\Gamma \cdot \mathbf{n} \; dn, \\ &= \frac{D}{P} \mathbf{f}_t(\mathbf{x}_\Gamma) \cdot \mathbf{n}, \end{aligned}$$

where we again use the assumption that flux $\mathbf{f}$ is zero along Γ and can therefore be pulled inside the integral over Γ.

Integrating the right-hand-side, we have:

$$\begin{aligned} \lim_{\epsilon \to 0} \int_{\gamma+\epsilon}^{\gamma-\epsilon} D \nabla(\nabla \cdot \mathbf{f}) \cdot \mathbf{n} \; dn &= D \lim_{\epsilon \to 0} \int_{\gamma+\epsilon}^{\gamma-\epsilon} \left[\frac{\partial}{\partial n}(\nabla \cdot \mathbf{f}) \mathbf{n} + \frac{\partial}{\partial \tau}(\nabla \cdot \mathbf{f}) \right] \cdot \mathbf{n} \; dn, \\ &= D \lim_{\epsilon \to 0} \int_{\gamma+\epsilon}^{\gamma-\epsilon} \left[\frac{\partial}{\partial n}(\nabla \cdot \mathbf{f}) \mathbf{n} + 0 \right] \cdot \mathbf{n} \; dn, \qquad (3.2.15) \end{aligned}$$

where τ is the variable in the tangential direction, n is the variable in the normal direction, and we use the assumption that there is no flux in the tangential direction. Simplifying and integrating (3.2.15), we have:

$$\begin{aligned} \lim_{\epsilon \to 0} \int_{\gamma+\epsilon}^{\gamma-\epsilon} D \nabla(\nabla \cdot \mathbf{f}) \cdot \mathbf{n} \; dn &= D \lim_{\epsilon \to 0} \int_{\gamma+\epsilon}^{\gamma-\epsilon} \frac{\partial}{\partial n}(\nabla \cdot \mathbf{f}) \mathbf{n} \cdot \mathbf{n} \; dn, \\ &= D \left[\nabla \cdot \mathbf{f} \Big|_{\gamma-\epsilon} - \nabla \cdot \mathbf{f} \Big|_{\gamma+\epsilon} \right], \\ &= D \left[\nabla \cdot \mathbf{f} \right]_\Gamma, \end{aligned}$$

where $[\,\cdot\,]_\Gamma$ denotes the jump across the interface as in condition (3.2.1). Combining results, we have:

$$0 + \frac{D}{P} \mathbf{f}_t \cdot \mathbf{n} = D \left[\nabla \cdot \mathbf{f} \right]_\Gamma .$$

Rearranging, we have the jump condition (3.2.11)

$$\mathbf{f} \cdot \mathbf{n} = P[\nabla \cdot \mathbf{f}]_\Gamma.$$

Having verified that the flux equation (3.2.12) is valid in the entire domain, we can now present the final model equations, where we have followed the work of Huang et al. [18]. The concentration c of particles, and the transmembrane flux $\mathbf{f}$, for $g(c) = c$, are given by the following coupled equations:

$$c_t = \nabla \cdot \left(D\nabla c + \int_\Gamma \frac{D\mathbf{f}}{P} \delta(\mathbf{x} - \mathbf{x}_\Gamma) d\mathbf{x}_\Gamma \right), \tag{3.2.16}$$

$$\mathbf{f}_t \left(1 + \int_\Gamma \frac{D}{P} \delta(\mathbf{x} - \mathbf{x}_\Gamma) d\mathbf{x}_\Gamma \right) = D\nabla(\nabla \cdot \mathbf{f}). \tag{3.2.17}$$

The boundary condition for concentration on the outer boundaries is taken to be the Neumann homogeneous boundary condition,

$$\frac{\partial c}{\partial n} = \frac{\nabla c \cdot \mathbf{n}}{|\mathbf{n}|} = \nabla c \cdot \mathbf{n} = 0,$$

where $\frac{\partial c}{\partial n}$ is the normal derivative, $\mathbf{n}$ is the unit normal vector to the interface Γ, and $|\mathbf{n}| = 1$. In this way, diffusion is confined within the domain Ω in which we run our simulations.

We take Neumann boundary condition at the outer boundary because it facilitates studying the effect of the outer boundaries. One applicable scenario is in simulating diffusion on a domain restricted by some outer boundary, such as a microstructure surrounding a group of cells. We could make the domain size small and vary the simulation run time to study the effect of the outer boundary on the solution. This would provide insight, for example, into errors that can be accrued by considering diffusion times that are too long for a given area, i.e. in the case where the outer boundaries play a significant role.

This can be particularly important to consider when applying diffusion models in the interpretation of signals from MRI experiments over a given voxel size and diffusion time. By varying the domain size and run time, we can simulate different scenarios for short-time diffusion.

Alternatively, applying periodic boundary conditions would artificially represent an infinite domain. Furthermore, if the domain size is not chosen appropriately with periodic boundary conditions, it may lead to artificially long transport due to molecules passing through the outer boundaries.

The initial conditions for concentration and flux are chosen in our simulations based on the problem we are interested in modelling, and on the spatial dimension (i.e., 1D vs. 2D). We will mention briefly the initial conditions used in the presentation of results in Chapter 4. We now provide an overview of the discretisation of the governing equations used in our simulations.

3.3 Discretisation of Governing Equations

To discretise the governing equations in 1D and 2D, we use the Crank-Nicolson method, which replaces the partial derivatives with implicit finite differences. Specifically, the method uses central differencing in space, and the average of the forward and backward Euler methods at t^n and t^{n+1}. This method is second order accurate in time, and has been shown to be unconditionally stable for the diffusion equation (among others) [33]. However, oscillatory behaviour can occur if the ratio of time step Δt to the square of space step $\Delta \mathbf{x}$ is large [36], e.g., for the 1D diffusion equation $c_t = \alpha c_{xx}$, where α is the diffusion coefficient, the condition is:

$$\alpha \frac{\Delta t}{(\Delta x)^2} \leq \frac{1}{2}. \tag{3.3.1}$$

Note: this relation is not dependent upon the scale used in time and space since the units for Δt and Δx will cancel with the units of α (taken here to be the diffusion coefficient, with dimension time^{-1}space). This strict requirement on Δt can become prohibitive for small mesh size and dimensions greater than 1D; in such cases, alternative methods are often used (e.g. backward Euler method, or an explicit jump method [22]). We choose to use the Crank-Nicolson method despite this restriction because we use sufficiently small mesh sizes and do not consider dimensions higher than two. In 3D, one may still use this numerical scheme. However, small time steps may be required to maintain an acceptable numerical accuracy.

Furthermore, to ensure that the solutions do not blow up or approach negative solutions, we seek to satisfy the maximum principle (see [26]). For the Crank-Nicolson method, the maximum principle is satisfied if the ratio in (3.3.1) is ≤ 1 [26]. We also choose to use the Crank-Nicolson method because it is relatively easy to set up and is a good first step in developing more efficient numerical methods.

For a 1D problem, i.e., for $u = u(x)$, on the uniform grid $\{x_0, x_1, ..., x_N\}$ of grid size Δx and at uniformly spaced discrete times $\{t_0, t_1, ..., t_{n+1}\}$ where Δt is the step size, the implicit finite difference formulae used by the Crank-Nicolson method are:

$$u = \frac{U_l^{n+1} - U_l^n}{2},$$

$$\frac{\partial u}{\partial t} = \frac{U_l^{n+1} - U_l^n}{\Delta t},$$

$$\begin{aligned}\frac{\partial u}{\partial x} &= \frac{1}{2}\left(\frac{U_{l+1}^{n+1} - U_{l-1}^{n+1}}{2\Delta x} + \frac{U_{l+1}^{n} - U_{l-1}^{n}}{2\Delta x}\right), \\ &= \frac{1}{4\Delta x}\left(U_{l+1}^{n+1} - U_{l-1}^{n+1} + U_{l+1}^{n} - U_{l-1}^{n}\right),\end{aligned}$$

where U_l^n is the approximation of $u(x_l, t_n)$, where $x_l = x_0 + l\Delta x$ and $t_n = t_0 + n\Delta t$.

3.3.1 One-Dimensional

Using the Crank-Nicolson method to discretise (3.2.16) in 1D on the uniform grid $\{x_0, x_1, ..., x_N\}$ of grid size Δx and at uniformly spaced discrete times $\{t_0, t_1, ..., t_{n+1}\}$ where Δt is the step size, we have:

$$\begin{aligned}\frac{C_i^{n+1} - C_i^n}{\Delta t} &= \frac{D}{2(\Delta x)^2}\left(\left(C_{i+1}^{n+1} - 2C_i^{n+1} + C_{i-1}^{n+1}\right) + \left(C_{i+1}^{n} - 2C_i^{n} + C_{i-1}^{n}\right)\right) \\ &\quad + \frac{D\delta_{h,i}}{P}\left(\frac{1}{4\Delta x}\left(\left(F_{i+1}^{n+1} - F_{i-1}^{n+1}\right) + \left(F_{i+1}^{n} - F_{i-1}^{n}\right)\right)\right),\end{aligned}$$

where C is the vector of unknowns for concentration c, i is the spatial index, and n is the temporal index; that is, the i-th component of C^n is $C_i^n \approx C(x_i, t_n)$. $\delta_{h,i}$ is the discrete delta function at x_i, and the line integral over Γ vanishes in 1D for point interfaces $\Gamma = x_\Gamma$. We have also set $D(x_i) = D$ for the 1D tests, although in 2D we allow spatial dependence of D. We use the discrete form of $\delta(\mathbf{x}-\mathbf{x}_\Gamma)$ proposed by Peskin [28]:

$$\delta_{h,i} = \frac{1}{(2\Delta x_j)^d}\prod_{j=1}^{d}\left(1+\cos\frac{\pi(x_j - x_{\Gamma j})}{\Delta x_j}\right),$$

where d is the spatial dimension (1, 2, or 3), x_j is the j-th component of $\mathbf{x}_i$, $x_{\Gamma j}$ is the j-th component of $\mathbf{x}_\Gamma$ on the boundary, and $\delta_{h,i} = 0$ for $|x_j - x_{\Gamma j}| > \Delta x_j$. Rearranging and grouping terms, we have:

$$\begin{aligned}(1+2\xi)C_i^{n+1} - \xi(C_{i+1}^{n+1} + C_{i-1}^{n+1}) &= (1-2\xi)C_i^n + \xi(C_{i+1}^n + C_{i-1}^n)\\ &\quad + \frac{D\Delta t}{4P\Delta x}\delta_{h,i}(F_{i+1}^{n+1} - F_{i-1}^{n+1} + F_{i+1}^n - F_{i-1}^n),\end{aligned}$$

where $\xi = \frac{D\Delta t}{2(\Delta x)^2}$. In the 1D problem that we consider, we fix the value of concentration at $x = x_0$ and $x = x_N$ (the outer boundaries of the domain). Using these boundary conditions, we have the following system of equations in matrix-vector form:

$$\xi\begin{bmatrix}\xi^{-1}+2 & -1 & 0 & 0 & \cdots & 0\\ -1 & \xi^{-1}+2 & -1 & 0 & \cdots & 0\\ 0 & -1 & \xi^{-1}+2 & -1 & \ddots & \vdots\\ \vdots & \ddots & \ddots & \ddots & \ddots & 0\\ \vdots & \ddots & \ddots & \ddots & \ddots & -1\\ 0 & \cdots & \cdots & \cdots & -1 & \xi^{-1}+2\end{bmatrix}\begin{bmatrix}C_1^{n+1}\\ C_2^{n+1}\\ C_3^{n+1}\\ \vdots\\ \vdots\\ C_N^{n+1}\end{bmatrix}$$

$$= \xi\begin{bmatrix}\xi^{-1}-2 & 1 & 0 & 0 & \cdots & 0\\ 1 & \xi^{-1}-2 & 1 & 0 & \cdots & 0\\ 0 & 1 & \xi^{-1}-2 & 1 & \ddots & \vdots\\ \vdots & \ddots & \ddots & \ddots & \ddots & 0\\ \vdots & \ddots & \ddots & \ddots & \ddots & 1\\ 0 & \cdots & \cdots & \cdots & 1 & \xi^{-1}-2\end{bmatrix}\begin{bmatrix}C_1^{n}\\ C_2^{n}\\ C_3^{n}\\ \vdots\\ \vdots\\ C_N^{n}\end{bmatrix}$$

$$+ \quad \frac{D\Delta t}{4P\Delta x}\begin{bmatrix} 0 & \delta_1 & 0 & 0 & \cdots & 0 \\ -\delta_2 & 0 & \delta_2 & 0 & \cdots & 0 \\ 0 & -\delta_3 & 0 & \delta_3 & \ddots & \vdots \\ \vdots & \ddots & \ddots & \ddots & \ddots & 0 \\ \vdots & \ddots & \ddots & \ddots & \ddots & \delta_{N-1} \\ 0 & \cdots & \cdots & \cdots & -\delta_N & 0 \end{bmatrix}\begin{bmatrix} F_1^{n+1} \\ F_2^{n+1} \\ F_3^{n+1} \\ \vdots \\ \vdots \\ F_N^{n+1} \end{bmatrix}$$

$$+ \quad \frac{D\Delta t}{4P\Delta x}\begin{bmatrix} 0 & \delta_1 & 0 & 0 & \cdots & 0 \\ -\delta_2 & 0 & \delta_2 & 0 & \cdots & 0 \\ 0 & -\delta_3 & 0 & \delta_3 & \ddots & \vdots \\ \vdots & \ddots & \ddots & \ddots & \ddots & 0 \\ \vdots & \ddots & \ddots & \ddots & \ddots & \delta_{N-1} \\ 0 & \cdots & \cdots & \cdots & -\delta_N & 0 \end{bmatrix}\begin{bmatrix} F_1^{n} \\ F_2^{n} \\ F_3^{n} \\ \vdots \\ \vdots \\ F_N^{n} \end{bmatrix} + 2\xi \begin{bmatrix} C_0 \\ 0 \\ \vdots \\ \vdots \\ 0 \\ C_1 \end{bmatrix},$$

where C_0 and C_1 are the values of concentration fixed at x_0 and x_1 respectively.

Using the Crank-Nicolson method to discretise the flux equation (3.2.17) in 1D, we have:

$$\frac{F_i^{n+1} - F_i^n}{\Delta t}(1 + \frac{D}{P}\delta_{h,i}) = \frac{D}{2(\Delta x)^2}\left(F_{i+1}^{n+1} - 2F_i^{n+1} + F_{i-1}^{n+1} + F_{i+1}^{n} - 2F_i^{n} + F_{i-1}^{n}\right).$$

Rearranging and grouping terms, we have:

$$\left((1 + \frac{D}{P}\delta_{h,i}) + 2\xi\right)F_i^{n+1} - \xi\left(F_{i+1}^{n+1} + F_{i-1}^{n+1}\right) = \left((1 + \frac{D}{P}\delta_{h,i}) - 2\xi\right)F_i^{n} + \xi\left(F_{i+1}^{n} + F_{i-1}^{n}\right).$$

At the outer boundaries, flux will be given by Fick's first law (3.3.2),

$$f = -D\nabla c. \qquad (3.3.2)$$

In particular, we use a finite difference approximation of (3.3.2) to calculate flux at the outer boundaries. Using this as the boundary condition for flux, we have the following system of equations in matrix-vector form:

$$\xi \begin{bmatrix} \Upsilon_1+2 & -1 & 0 & 0 & \cdots & 0 \\ -1 & \Upsilon_2+2 & -1 & 0 & \cdots & 0 \\ 0 & -1 & \Upsilon_3+2 & -1 & \ddots & \vdots \\ \vdots & \ddots & \ddots & \ddots & \ddots & 0 \\ \vdots & \ddots & \ddots & \ddots & \ddots & -1 \\ 0 & \cdots & \cdots & \cdots & -1 & \Upsilon_N+2 \end{bmatrix} \begin{bmatrix} F_1^{n+1} \\ F_2^{n+1} \\ F_3^{n+1} \\ \vdots \\ \vdots \\ F_N^{n+1} \end{bmatrix}$$

$$= \xi \begin{bmatrix} \Upsilon_1-2 & 1 & 0 & 0 & \cdots & 0 \\ 1 & \Upsilon_2-2 & 1 & 0 & \cdots & 0 \\ 0 & 1 & \Upsilon_3-2 & 1 & \ddots & \vdots \\ \vdots & \ddots & \ddots & \ddots & \ddots & 0 \\ \vdots & \ddots & \ddots & \ddots & \ddots & 1 \\ 0 & \cdots & \cdots & \cdots & 1 & \Upsilon_N-2 \end{bmatrix} \begin{bmatrix} F_1^{n} \\ F_2^{n} \\ F_3^{n} \\ \vdots \\ \vdots \\ F_N^{n} \end{bmatrix} + 2\xi \begin{bmatrix} F_0 \\ 0 \\ \vdots \\ \vdots \\ 0 \\ F_1 \end{bmatrix},$$

where $\Upsilon_i = (1 + \frac{D}{P}\delta_i)\xi^{-1}$ for $i = 1, 2, ...N$, and F_0 and F_1 are the values of flux at x_0 and x_N respectively, calculated from (3.3.2) based on fixed values of concentration at the boundaries. In the 1D numerical test we present in Chapter 4, we compare our numerical solution with an analytical solution for steady-state concentration. To pre-compute the values for F_0 and F_1 and use them as the flux boundary conditions, we use the steady-state solution and plug into (3.3.2) the values of concentration for two points near each of the boundaries.

Having demonstrated the discretisation of (3.2.16) and (3.2.17) in one dimension, we now go into similar detail for the discretisation in two dimensions.

3.3.2 Two-Dimensional

The discretisation of the governing equations in two or more dimensions adds a greater level of complexity, not only in the size of matrices, but also in the details of the numerical methods used. For example, we now integrate along the interface Γ, whereas the interfaces are single points in 1D. In addition, the flux variable is now vector valued. To demonstrate the discretisation, we present our numerical methods for two dimensions, where it is a straightforward extension to apply the methods for three-dimensions.

For our simulation domain, we choose $\Delta x = \Delta y$ on a square domain, where time t is discretised into points $n = 0, 1, 2, ...,$ x is discretised into points x_i for $i = 0, 1, ..., N$, and y is discretised into points y_j for $j = 0, 1, ..., N$. Using the Crank-Nicolson method to discretise (3.2.16), we have:

$$\frac{C_{i,j}^{n+1} - C_{i,j}^{n}}{\Delta t} = \frac{1}{2(\Delta x)^2}[(D_{i+1,j}C_{i+1,j}^{n+1} + D_{i-1,j}C_{i-1,j}^{n+1} + D_{i,j+1}C_{i,j+1}^{n+1} + D_{i,j-1}C_{i,j-1}^{n+1}$$
$$-4D_{i,j}C_{i,j}^{n+1})] + \frac{1}{2(\Delta x)^2}[(D_{i+1,j}C_{i+1,j}^{n} + D_{i-1,j}C_{i-1,j}^{n} + D_{i,j+1}C_{i,j+1}^{n} + D_{i,j-1}C_{i,j-1}^{n}$$
$$-4D_{i,j}C_{i,j}^{n})] + S_{i,j},$$

where $S_{i,j}$ is the discretised version of the integral term in (3.2.16). We will discuss this term below.

Rearranging and grouping terms, we have:

$$(1 + (2\mu)D_{i,j})C_{i,j}^{n+1} - \frac{\mu}{2}(D_{i+1,j}C_{i+1,j}^{n+1} + D_{i-1,j}C_{i-1,j}^{n+1} + D_{i,j+1}C_{i,j+1}^{n+1} + D_{i,j-1}C_{i,j-1}^{n+1})$$
$$= (1 - (2\mu)D_{i,j})C_{i,j}^{n} + \frac{\mu}{2}(D_{i+1,j}C_{i+1,j}^{n} + D_{i-1,j}C_{i-1,j}^{n} + D_{i,j+1}C_{i,j+1}^{n} + D_{i,j-1}C_{i,j-1}^{n}), \quad (3.3.3)$$

where $\mu = \frac{\Delta t}{(\Delta x)^2}$. To simplify and condense the notation for indices, we use the following index scheme:

$$C_{l-1} = C_{i-1,j}, \qquad C_l = C_{i,j}, \qquad C_{l+1} = C_{i+1,j},$$
$$C_{l-M} = C_{i,j-1}, \qquad C_{l+M} = C_{i,j+1}.$$

Substituting these indices into (3.3.3), we have:

$$(1 + (2\mu)D_l)C_l^{n+1} - \frac{\mu}{2}(D_{l+1}C_{l+1}^{n+1} + D_{l-1}C_{l-1}^{n+1} + D_{l+N}C_{l+N}^{n+1} + D_{l-N}C_{l-N}^{n+1})$$
$$= (1 - (2\mu)D_l)C_l^{n} + \frac{\mu}{2}(D_{l+1}C_{l+1}^{n} + D_{l-1}C_{l-1}^{n} + D_{l+N}C_{l+N}^{n} + D_{l-N}C_{l-N}^{n}) \quad . (3.3.4)$$

Using this five-point stencil, we require values of concentration at ‘ghost points’ - points outside of the computational mesh of x_i and y_j points. Since these points do not exist, we may use the Neumann homogeneous boundary condition,

$$\frac{\partial c}{\partial n} = \nabla c \cdot \mathbf{n} = 0,$$

to write equations for concentration at these ghost points outside the outer walls. First, rearranging the Neumann homogeneous boundary condition and substituting the (outward) unit normal vector $\mathbf{n}$ for each of the outer boundaries produces the following equations:

$$\tfrac{\partial c}{\partial n} = -\tfrac{\partial c}{\partial y} = 0, \qquad \tfrac{\partial c}{\partial n} = \tfrac{\partial c}{\partial y} = 0,$$

$$\tfrac{\partial c}{\partial n} = -\tfrac{\partial c}{\partial x} = 0, \qquad \tfrac{\partial c}{\partial n} = \tfrac{\partial c}{\partial x} = 0,$$

for the bottom, top, left, and right boundaries, respectively (reading from the top left to the bottom right). Using second order differencing, the discretised boundary conditions are:

$$\frac{\partial c}{\partial x} = \frac{c_{i+1,j} - c_{i-1,j}}{2\Delta x} = 0, \quad \frac{\partial c}{\partial y} = \frac{c_{i,j+1} - c_{i,j-1}}{2\Delta y} = 0. \tag{3.3.5}$$

Solving for concentration and using the indices in l, we have

$$c_{l-N} = c_{l+N}, \qquad c_{l+N} = c_{l-N},$$

$$c_{l-1} = c_{l+1}, \qquad c_{l+1} = c_{l-1}.$$

Finally, we must substitute these boundary conditions into (3.3.4) to remove the ghost points on each of the outer boundaries. This is a tedious, but straightforward, step which we will not demonstrate here for the four outer boundaries and four corners.

For a $N \times N$ computational mesh, we have N^2 unknowns: $c_1, c_2, \dots c_{N\times N}$. We solve a system of N^2 equations to obtain N^2 unknowns. To do so, we solve the system of equations simultaneously by first writing it in terms of matrix-vector products. The size and complexity of the matrix-vector form is too great to represent here, so will write the system compactly as

$$\mathrm{B_1 C^{n+1} = B_0 C^n},$$

where B_0, B_1 are $N^2 \times N^2$ matrices, and C^n is the $N^2 \times 1$ vector of unknowns.

Next, we discretise the integral term from (3.2.16),

$$\nabla \cdot \left(\int_\Gamma \frac{D\mathbf{f}}{P} \delta(\mathbf{x} - \mathbf{x}_\Gamma) d\mathbf{x}_\Gamma \right) =$$

$$\left(\frac{\partial}{\partial x}, \frac{\partial}{\partial y} \right) \cdot \left(\frac{D}{P} \int_\Gamma g(x,y) \delta(\mathbf{x} - \mathbf{x}_\Gamma) d\mathbf{x}_\Gamma, \frac{D}{P} \int_\Gamma h(x,y) \delta(\mathbf{x} - \mathbf{x}_\Gamma) d\mathbf{x}_\Gamma \right), \tag{3.3.6}$$

where we let $\mathbf{f} = (g(x,y), h(x,y))$ be the vector-valued flux in two dimensions.

Applying the Crank-Nicolson method to (3.3.6), and combining with (3.3.4), we have:

$$\begin{aligned}
(1 + (2\mu)D_l)C_l^{n+1} - \frac{\mu}{2}(D_{l+1}C_{l+1}^{n+1} + D_{l-1}C_{l-1}^{n+1} + D_{l+N}C_{l+N}^{n+1} + D_{l-N}C_{l-N}^{n+1}) \\
= (1 - (2\mu)D_l)C_l^n + \frac{\mu}{2}(D_{l+1}C_{l+1}^n + D_{l-1}C_{l-1}^n + D_{l+N}C_{l+N}^n + D_{l-N}C_{l-N}^n) + \\
\frac{\Delta t}{4\Delta x}\left[(G_{l+1}^{n+1} I_{l+1}^{n+1} - G_{l-1}^{n+1} I_{l-1}^{n+1}) + (G_{l+1}^n I_{l+1}^n - G_{l-1}^n I_{l-1}^n) \right] + \\
\frac{\Delta t}{4\Delta x}\left[(H_{l+1}^{n+1} I_{l+1}^{n+1} - H_{l-1}^{n+1} I_{l-1}^{n+1}) + (H_{l+1}^n I_{l+1}^n - H_{l-1}^n I_{l-1}^n) \right],
\end{aligned}$$

where

$$I_l = \frac{D_l}{P} \sum_{k=1}^{\tilde{M}-1} \Delta s \; \delta_{h,l}(\mathbf{x}_l - \mathbf{x}_{\Gamma,k}),$$

(using the trapezoidal rule for numerical integration over a closed path Γ), $\tilde{M}$ is the number of points along the interface Γ, Δs (weighting factor) is chosen to be the arc length of the interface, and

$$\delta_{h,l}(X_k, Y_k) = \frac{1}{(2\Delta x)^2} \left(1 + \cos \frac{\pi(x_i - X_k)}{\Delta x} \right) \left(1 + \cos \frac{\pi(y_j - Y_k)}{\Delta x} \right), \tag{3.3.7}$$

if $|x_i - X_k| \leq \Delta x$ and $|y_j - Y_k| \leq \Delta x$.

The flux on the outer boundary is zero everywhere because of the Neumann homogeneous boundary condition for concentration. As such, no extra terms are needed for the flux boundary conditions, and we can remove the ghost points by setting flux equal to zero on the boundary. The matrix-vector form of this system of equations can be expressed compactly as:

$$B_1 C^{n+1} = B_0 C^n + D_1 \left(G^{n+1} + G^n\right) + D_2 \left(H^{n+1} + H^n\right),$$

where B_1, B_0, D_1, D_2 are $N^2 \times N^2$ matrices, C^n is the $N^2 \times 1$ concentration vector of unknowns, and G^n, H^n are the $N^2 \times 1$ vectors of unknowns for flux in the x- and y-directions, respectively.

Using linear solvers in MATLAB, we solve the system for C^{n+1} given the approximate values for the horizontal and vertical components of flux $\mathbf{f}$, (G, H), found as described below, and the approximate values of c at t_n stored in C^n.

To solve for $\mathbf{f} = (g(x,y), h(x,y))$ in (3.2.17), we have two governing equations, which we discretise separately:

$$g_t \left(1 + \int_\Gamma \frac{D}{P} \delta(x - x_\Gamma) dx_\Gamma\right) = D \frac{\partial}{\partial x}\left(\frac{\partial g}{\partial x} + \frac{\partial h}{\partial y}\right) = D \left(\frac{\partial^2 g}{\partial x^2} + \frac{\partial^2 h}{\partial x \partial y}\right), \qquad (3.3.8)$$

$$h_t \left(1 + \int_\Gamma \frac{D}{P} \delta(y - y_\Gamma) dy_\Gamma\right) = D \frac{\partial}{\partial y}\left(\frac{\partial g}{\partial x} + \frac{\partial h}{\partial y}\right) = D \left(\frac{\partial^2 g}{\partial y \partial x} + \frac{\partial^2 h}{\partial y^2}\right). \qquad (3.3.9)$$

Using the Crank-Nicolson method to discretise (3.3.8), we have:

$$\begin{aligned}\frac{G_l^{n+1} - G_l^n}{\Delta t}\eta_l = {} & \frac{D}{2(\Delta x)^2}\left[G_{l+1}^{n+1} - 2G_l^{n+1} + G_{l-1}^{n+1} + \frac{H_{l+M+1}^{n+1} - H_{l-M+1}^{n+1} - H_{l+M-1}^{n+1} + H_{l-M-1}^{n+1}}{4}\right] \\ & + \frac{D}{2(\Delta x)^2}\left[G_{l+1}^{n} - 2G_l^{n} + G_{l-1}^{n} + \frac{H_{l+M+1}^{n} - H_{l-M+1}^{n} - H_{l+M-1}^{n} + H_{l-M-1}^{n}}{4}\right], \qquad (3.3.10)\end{aligned}$$

where

$$\eta_l = 1 + \frac{D_l \Delta s}{P}\left[\frac{\delta_{h,l}(\mathbf{x}_l - X_{\Gamma,1}) - \delta_{h,l}(\mathbf{x}_l - X_{\Gamma,N})}{2} + \sum_{k=2}^{N-1} \delta_{h,l}(\mathbf{x}_l - X_{\Gamma,k})\right]$$

is the discretisation of the integral part from (3.3.8) and (3.3.9), the discrete delta function $\delta_{h,l}$ is given by (3.3.7), and the diffusion coefficient $D(x,y)$ is written as D for ease of reading, although in practice, we replace $D(\mathbf{x}_l)$ with D_l in the discretisation. Similarly, the discretisation of (3.3.9) is:

$$\begin{aligned}\frac{H_l^{n+1}-H_l^n}{\Delta t}\eta_l &= \frac{D}{2(\Delta x)^2}\left[\frac{G_{l+M+1}^{n+1}-G_{l-M+1}^{n+1}-G_{l+M-1}^{n+1}+G_{l-M-1}^{n+1}}{4}+H_{l+M}^{n+1}-2H_l^{n+1}+H_{l-M}^{n+1}\right]\\ &+\frac{D}{2(\Delta x)^2}\left[\frac{G_{l+M+1}^{n}-G_{l-M+1}^{n}-G_{l+M-1}^{n}+G_{l-M-1}^{n}}{4}+H_{l+M}^{n}-2H_l^{n}+H_{l-M}^{n}\right]. \quad (3.3.11)\end{aligned}$$

Rearranging and grouping terms for (3.3.10) we have:

$$\begin{aligned}(\eta_l+\mu D_l)\,G_l^{n+1}-\frac{\mu}{2}\left(D_{l+1}G_{l+1}^{n+1}+D_{l-1}G_{l-1}^{n+1}\right) &= (\eta_l-\mu D_l)\,G_l^{n}+\frac{\mu}{2}\left(D_{l+1}G_{l+1}^{n}+D_{l-1}G_{l-1}^{n+1}\right)\\ &+\frac{\mu}{8}\left[\left(D_{l+M+1}H_{l+M+1}^{n+1}-D_{l-M+1}H_{l-M+1}^{n+1}-D_{l+M-1}H_{l+M-1}^{n+1}+D_{l-M-1}H_{l-M-1}^{n+1}\right)\right]\\ &+\frac{\mu}{8}\left[\left(D_{l+M+1}H_{l+M+1}^{n}-D_{l-M+1}H_{l-M+1}^{n}-D_{l+M-1}H_{l+M-1}^{n}+D_{l-M-1}H_{l-M-1}^{n}\right)\right],\end{aligned}$$

where

$$\mu=\frac{\Delta t}{(\Delta x)^2}.$$

Similarly, rearranging and grouping terms for (3.3.11) we have:

$$\begin{aligned}&(\eta_l+\mu D_l)\,H_l^{n+1}-\frac{\mu}{2}\left(D_{l+M}H_{l+M}^{n+1}+D_{l-M}H_{l-M}^{n+1}\right)\\ &=(\eta_l-\mu D_l)\,H_l^{n}+\frac{\mu}{2}\left(D_{l+M}H_{l+M}^{n}+D_{l-M}H_{l-M}^{n+1}\right)\\ &+\frac{\mu}{8}\left[\left(D_{l+M+1}G_{l+M+1}^{n+1}-D_{l-M+1}G_{l-M+1}^{n+1}-D_{l+M-1}G_{l+M-1}^{n+1}+D_{l-M-1}G_{l-M-1}^{n+1}\right)\right]\\ &+\frac{\mu}{8}\left[\left(D_{l+M+1}G_{l+M+1}^{n}-D_{l-M+1}G_{l-M+1}^{n}-D_{l+M-1}G_{l+M-1}^{n}+D_{l-M-1}G_{l-M-1}^{n}\right)\right].\end{aligned}$$

The matrix-vector form of these two systems of equations can be expressed compactly as:

$$\begin{aligned}E_1G^{n+1} &= E_0G^n+G_1\left(H^{n+1}+H^n\right), \quad \text{and}\\ F_1H^{n+1} &= F_0H^n+G_1\left(G^{n+1}+G^n\right),\end{aligned}$$

where E_1, E_0, F_0, F_1, and G_1 are $N^2\times N^2$ matrices. Using linear solvers in MATLAB, we solve for G^{n+1} and H^{n+1}, and substitute these into our system of equations for

C^{n+1}.

Now that we have a numerical scheme for solving the governing equations, we present simulations for some one- and two-dimensional problems. We will provide a second numerical technique that uses strictly finite difference equations (without the IB method framework) to validate our proposed numerical scheme. By comparing the results from both methods, we may demonstrate that the immersed boundary method is a viable technique for modelling diffusion in cellular media.

Chapter 4

Numerical Tests and Validation

We present some numerical tests to establish the proposed immersed boundary (IB) method's applicability to simulating diffusion in cellular media. Specifically, we are interested in the simulations of diffusion in cellular media involving semipermeable membranes and diffusion coefficients D_I and D_O (interior and exterior, respectively) that are not necessarily equal. Using the model equations presented in Chapter 2, and the numerical schemes outlined in Chapter 3, we run simulations in one and two dimensions.

In Section 4.1, we consider a simple one-dimensional problem for which we have an analytical solution (at equilibrium). In Section 4.2.1, we present a second numerical scheme in which we discretise the governing equations using standard finite differences, without using the IB method framework. This finite difference (FD) method is used in Section 4.2.2 to validate the IB method in the absence of an analytical solution.

Because of the difficulty in deriving the FD method, we only consider a square interface in our comparisons. In Section 4.3, we demonstrate the flexibility and power of the IB method framework by presenting simulations for a variety of interface shapes, including ellipses, and groups of circles.

In both one and two dimensions, we present qualitative and quantitative comparisons between two sets of solutions to reveal the strengths and weaknesses of the proposed IB method. One quantitative assessment we present is a convergence analysis to test the accuracy of our numerical method. To calculate the order of convergence, we first calculate L_2 errors,

$$E = \sqrt{\frac{1}{N^d}\sum_{i=1}^{N^d}(c_i - \tilde{c}_i)^2}, \tag{4.0.1}$$

where N is the number of computational grid points in each dimension d, and c_i is the exact solution at the i-th grid point. When comparing the computations on the two dimensional grid, we do not know the exact solution and therefore approximate c_i using $\bar{c}_i$, the numerical solution at the i-th grid point using $N = 200$. $\tilde{c}_i$ is the numerical solution at $N = 25, 50$, or 100, where, for the computations in 1D, we also use $N = 200$ and $N = 400$. The order of convergence, then, is

$$p = \frac{\log(\frac{E_1}{E_2})}{\log(2)}, \tag{4.0.2}$$

where E_1 and E_2 are two successive L_2 errors calculated for N_1 and N_2, respectively, with $N_1 = \frac{1}{2}N_2$.

In the following numerical tests, we will present a convergence analysis for the simulations in one and two dimensions and discuss what the implications are for the accuracy of the IB method. We will also present the qualitative behaviour of the IB method by comparing the numerical solutions to the analytical solution in one dimension, and likewise to the FD method solutions in two dimensions.

4.1 One-Dimensional Tests

In the following numerical tests, we consider a simple one-dimensional problem for which we have an analytical solution. The diffusion equation in 1D is:

$$c_t = D\, c_{xx}, \tag{4.1.1}$$

where D is the diffusion coefficient. We consider two interfaces of permeability P located at points x_1 and x_2, and fix the concentration to be $c_0 = 2.0$ and $c_1 = 1.0$ at the two ends of the interval $x \in [0,1]$. The boundary conditions at the interfaces are given by the linear flux law,

$$Dc_x = P[c]_\Gamma, \tag{4.1.2}$$

where $[\,\cdot\,]_\Gamma$ denotes the jump across the interface.

The analytical steady-state solution to (4.1.1) can be found by solving $c_{xx} = 0$ for the three regimes, separated at x_1 and x_2. If we denote concentration in the first, second, and third regime by $c^{(1)}$, $c^{(2)}$, and $c^{(3)}$, respectively, then the boundary conditions are:

1. $c^{(1)}(0) = c_0$
2. $c^{(3)}(1) = c_1$
3. $Dc_x^{(1)}(x_1) = P[c^{(1)}(x_1) - c^{(2)}(x_1)]$
4. $Dc_x^{(2)}(x_1) = P[c^{(1)}(x_1) - c^{(2)}(x_1)]$
5. $Dc_x^{(2)}(x_2) = P[c^{(2)}(x_2) - c^{(3)}(x_2)]$
6. $Dc_x^{(3)}(x_2) = P[c^{(2)}(x_2) - c^{(3)}(x_2)]$.

The analytical steady-state solution will satisfy these boundary conditions, and is given by:

$$c = \begin{cases} mx + c_0, & x < x_1; \\ mx + c_m, & x_1 \leq x < x_2; \\ m(x-1) + c_1, & x \geq x_2, \end{cases} \tag{4.1.3}$$

where the constants

$$m = \frac{c_1 - c_0}{2DP^{-1} + 1}, \quad \text{and } c_m = \frac{DP^{-1}(c_0 + c_1) + c_0}{2DP^{-1} + 1},$$

are found from imposing the linear flux law (4.1.2) at the interface Γ [18].

Note that we do not consider a discontinuous diffusion coefficient in our one-dimensional numerical tests as we did not derive an analytical solution for such a problem. However, the numerical tests in two dimensions do implement a discontinuous diffusion coefficient since this is an important physical property of biological tissues.

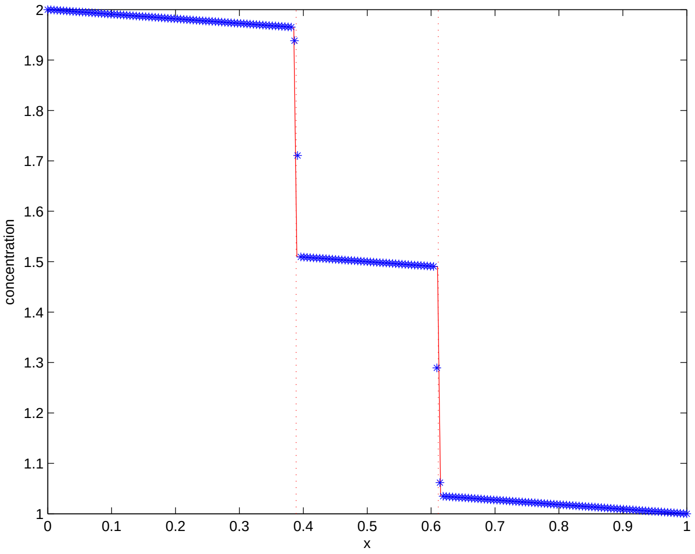

Figure 4.1: Steady-state solutions for a one-dimensional problem with concentration fixed at both ends and two immersed interfaces located at $x_1 = 7/18$ and $x_2 = 11/18$. The analytical solution is represented by a solid line, the numerical solution is plotted as $*$ points, and the vertical dashed lines mark the locations of the immersed interfaces. The cellular parameters used are $D = 1.0$ µm^2/ms and $P = 0.02$ µm/ms.

4.1.1 Qualitative Comparison of Analytical and Numerical Solutions

In Figure 4.1 we plot the numerical and analytical steady-state solutions for a simulation where the cellular parameters are chosen to be $D = 1.0$ µm^2/ms and $P = 0.02$ µm/ms. For the computational mesh, we use $\Delta x = 0.02, N = 200$ points along x, and $\Delta t = 0.001$. The analytical solution is represented by a solid line and the numerical solution is plotted as $*$ points.

The numerical solution is considered to have reached steady-state once the flux f throughout the entire domain is a constant value. In Figure 4.2, the flux is plotted (left) for a non-steady-state solution, as well as the delta function $\delta(x - x_i)$.

In Figure 4.1, we see that the numerical and analytical solutions are qualitatively quite similar. The greatest discrepancies between the two methods are at the interfaces x_1 and x_2, as can be seen in the graph of relative error $|c_i - \tilde{c}_i|$, plotted in Figure 4.3.

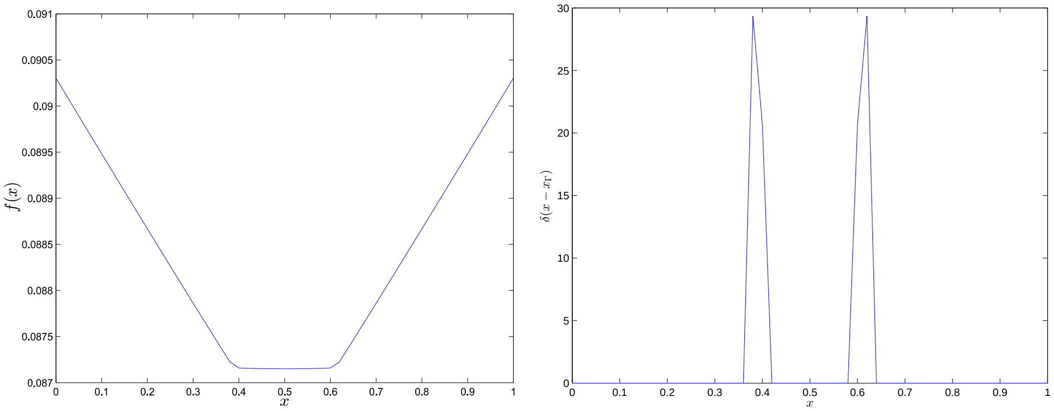

Figure 4.2: The flux f (left) and delta function δ (right) for the non-steady-state solution using the immersed boundary method in one dimension.

This may be due to the finite representation of the delta function, $\delta_h(x - x_i)$, which is used in the discretisation of the IB method governing equations, (3.2.16) and (3.2.17). In the limit $\lim_{\Delta x \to 0} \Delta x$, the maximum value of the discrete delta function approaches infinity, which leads to a sharper drop in concentration at the interface Γ. Therefore, we expect that the numerical solution would more closely match the analytical solution at the interface as Δx is decreased.

Furthermore, we use finite differences to discretise the derivatives of concentration and flux at the interface. This approach is known to reduce the order of accuracy when applied to problems involving discontinuities in the analytical solution. We will discuss this further when we present the following convergence tests for the IB method.

4.1.2 Convergence Analysis

Using equation (4.0.2), we calculate the orders of convergence for the previous one-dimensional diffusion problem. We choose the diffusion coefficient $D = 1.0\,\mu\text{m}^2/\text{ms}$ and test different values of permeability P. We choose the analytical solution as the exact solution, and present the convergence results in Table 4.1 for N=25, 50, 100, 200, and 400 points.

For the IB method, we observe approximate first-order convergence rates. Further-

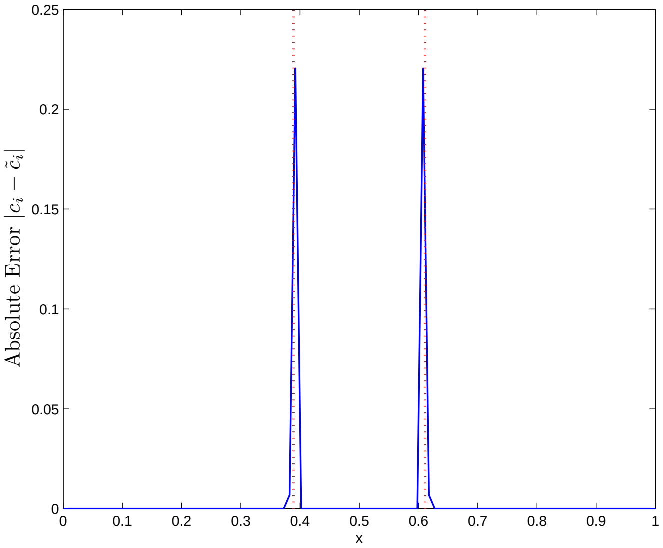

Figure 4.3: Absolute error $|c_i - \tilde{c}_i|$ for the 1D immersed boundary method, where c_i is the exact steady-state solution, $\tilde{c}$ is the numerical solution, and we use $D = 1.0\,\mu\text{m}^2/\text{ms}$, $P = 0.02\,\mu\text{m/ms}$, and N=100. The error is largest at the two interfaces located at $x_1 = 7/18$ and $x_2 = 11/18$.

more, the rate of convergence gets much worse as permeability P decreases. This is because the finite differences used in the discretisation of derivatives introduce significant errors into the numerical solution for small P. As P decreases, the discontinuity in the solution for concentration c becomes more apparent at the interface Γ. The numerical scheme therefore converges more slowly to the numerical solution as more points are needed to accurately represent the jump in concentration using the finite difference discretisation.

In general, the approximately first-order convergence rates are expected because of the nonsmoothness of concentration at the interface Γ. In fact, immersed boundary methods are known to produce first-order rates of convergence because they are often applied to problems whose true solutions are not smooth [14]. For example, many fluid-structure problems to which IB methods are applied involve an infinitely thin membrane, which are not sufficiently regular to achieve second-order convergence rates.

There are related methods, such as the class of immersed interface methods [41, 23], that have observed higher order convergence rates. Note that these have been applied to elliptic problems, and are generally much more difficult to set up than the immersed boundary method. One immersed boundary method that has observed second-order convergence rates is that by Peskin and Griffith [14], in which they consider an interface of finite thickness. In this case, the solution is sufficiently smooth to achieve second-order accuracy.

Table 4.1: Orders of convergence, p, for the IB method in one dimension. Here, the cellular parameters used are $D = 1.56\,\mu\text{m}^2/\text{ms}$ and $P = 0.01\,\mu\text{m/ms}$, $1.0\,\mu\text{m/ms}$, and $100\,\mu\text{m/ms}$.

	P=0.01		P=1.0		P=100	
N	$\lVert L_2 \rVert$	p	$\lVert L_2 \rVert$	p	$\lVert L_2 \rVert$	p
25	6.6044E-02		2.0364E-02		2.2171E-02	
50	4.7153E-02	0.49	1.1276E-02	0.85	1.1302E-02	0.97
100	3.3506E-02	0.49	7.2307E-03	0.64	5.7021E-03	0.99
200	2.3751E-02	0.50	4.3432E-03	0.74	2.8656E-03	0.99
400	1.6815E-02	0.50	2.4225E-03	0.84	1.4370E-03	1.00

Despite the approximate first-order convergence, we do however have good qualitative behaviour using the IB method in one dimension, as shown in the example presented in Section 4.1.1. We will now present numerical tests for the IB method in two dimensions to test the validity and accuracy of the proposed method for diffusion in cellular media.

4.2 Two-Dimensional Tests

We now consider simulations for our cellular diffusion model in two dimensions. Because an analytical solution is not available, and we wish to validate the proposed immersed boundary (IB) method, we implement a second numerical method based on a standard finite difference (FD) scheme. This FD method uses the Crank-Nicolson method in its discretisation, but does not use the IB method framework to impose the effect of the interface. Instead, the flux law (4.2.2) is imposed at the interface Γ as a boundary condition. This is relatively easy to do because the immersed interface we consider in our numerical tests is square and lies on the computational grid. Standard finite differences can then be used and still achieve second-order convergence, as demonstrated in the following tests.

4.2.1 Finite Difference (FD) Scheme

The standard diffusion equation in a homogeneous medium is

$$c_t = \nabla \cdot (D \nabla c)\,, \tag{4.2.1}$$

where c is the concentration of particles and D is the diffusion coefficient. In the discretisation of (4.2.1) using the FD method, we formally consider the concentration inside and outside the interface separately, allowing us to produce a discontinuity in concentration in our numerical solution at the interface Γ.

We accomplish this by first separating the computational grid points into two sets: $\mathbf{X}_O$, those that are outside or exactly on the interface; and $\mathbf{X}_I$, those that are inside or exactly on the interface. We therefore split the domain Ω into regions Ω_{out} and Ω_{in}, where Ω_{out} is defined as $(\Omega \setminus \Omega_{\text{in}}) \cup \Gamma$ (see Figure 4.4). The grid points in Ω_{out} form the set $\mathbf{X}_O$, and those in Ω_{in} form the set $\mathbf{X}_I$. Between $\mathbf{X}_O$ and $\mathbf{X}_I$, there is an overlap of points at the interface Γ, meaning that we will have two values of concentration at each grid point that is aligned with the interface. In Figure 4.4, the points that overlap, i.e., those on the interface Γ, are represented as bold circles, and the smaller circles represent the remaining points in $\mathbf{X}_I$.

To impose the effect of the interface on the numerical solution, we use the following boundary condition at Γ:

$$D \nabla c = P\,[c]_\Gamma\,\mathbf{n}, \tag{4.2.2}$$

where P is the membrane permeability, $[\,\cdot\,]_\Gamma$ denotes the jump across the interface, and $\mathbf{n}$ is the unit normal vector of the interface. The boundary condition used on the outer walls of Ω is the Neumann homogeneous boundary condition,

$$\frac{\partial c}{\partial n} = \nabla c \cdot \mathbf{n} = 0. \tag{4.2.3}$$

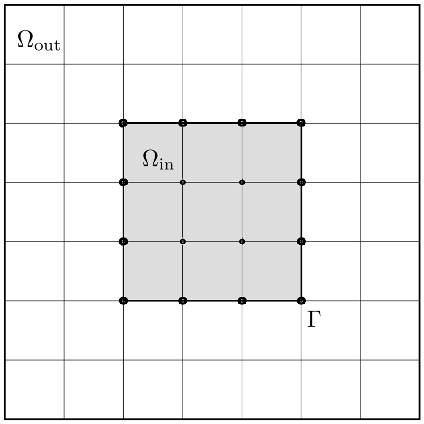

Figure 4.4: For the finite difference (FD) method, concentration is solved separately for each of the subdomains, Ω_{out} and Ω_{in}. These correspond to regions outside and inside the cell, respectively. Boundary conditions are used on the interface Γ, to model the effect of the semipermeable membrane.

We use the Crank-Nicolson method to discretise equations (4.2.1), (4.2.2), and (4.2.3), and approximate the solution to c at each of the points in $\mathbf{X}_O$ and $\mathbf{X}_I$.

To simultaneously solve for concentration in the entire domain Ω, we form a single set of unknowns for concentration. First, we denote C_l^n and $\tilde{C}_m^n$ as the approximate solutions generated at grid points $l = 0, 1, ..., N$ and $m = 0, 1, ..., N$ in $\mathbf{X}_O$ and $\mathbf{X}_I$, respectively, at time t_n, where $n = 0, 1, ...$ We combine C_l^n and $\tilde{C}_m^n$ into a single column vector U with elements U_k^n. For N points in the x direction, N points in the y direction, and M points along the interface, $k = 1, 2, ..., N^2 + M$.

Figure 4.5 illustrates a computational grid involving $N = 8$ points in the x and y directions, and $M = 12$ points on the interface Γ. This example has unknowns $\{C_1, C_2, ..., C_{60}\}$ and $\{\tilde{C}_1, \tilde{C}_2, ..., \tilde{C}_{16}\}$. The ordering of C_l^n and $\tilde{C}_m^n$ in the vector of unknowns U is in a bottom-up, left-to-right fashion, as demonstrated in Table 4.2 for some values of k. The five point stencil described below is also presented to further demonstrate the ordering of unknowns.

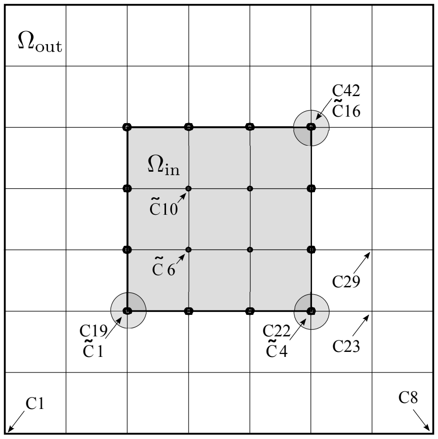

Figure 4.5: Illustration of the indexing system used for the vector of unknowns U for the finite difference (FD) method. This computational domain uses $N = 8$ points in the x and y directions, and $M = 12$ points on the interface Γ.

Discretising (4.2.1) using the Crank-Nicolson method for points in $\mathbf{X}_O$, we have:

$$\begin{aligned}&(1+4\xi_O)\,C_l^{n+1} - \xi_O\left(C_{l+1}^{n+1} + C_{l-1}^{n+1} + C_{l+N}^{n+1} + C_{l-N}^{n+1}\right)\\&= (1-4\xi_O)\,C_l^{n} + \xi_O\left(C_{l+1}^{n} + C_{l-1}^{n} + C_{l+N}^{n} + C_{l-N}^{n}\right),\end{aligned} \tag{4.2.4}$$

where $\xi_O = D_O\Delta t/h^2$, $h = \Delta x = \Delta y$ is the spatial mesh size, and D_O is the diffusion coefficient. For points in $\mathbf{X}_I$, we have:

$$\begin{aligned}&(1+4\xi_I)\,\tilde{C}_m^{n+1} - \xi_I\left(\tilde{C}_{m+1}^{n+1} + \tilde{C}_{m-1}^{n+1} + \tilde{C}_{m+M/3}^{n+1} + \tilde{C}_{m-M/3}^{n+1}\right)\\&= (1-4\xi_I)\,\tilde{C}_m^{n} + \xi_I\left(\tilde{C}_{m+1}^{n} + \tilde{C}_{m-1}^{n} + \tilde{C}_{m+M/3}^{n} + \tilde{C}_{m-M/3}^{n}\right),\end{aligned} \tag{4.2.5}$$

where $\xi_I = D_I\Delta t/h^2$, and D_I is the diffusion coefficient.

The five point stencil used here requires points outside of the computational grid, called ‘ghost points’. We use the homogeneous Neumann boundary condition at the outer boundary to remove the ghost points, as similarly used for the IB method in Section 3.3.2. At the interface Γ, we also have ghost points, which we remove using the interface flux law (4.2.2). Beginning with the ghost points at Γ, we use centered differences to approximate the spatial derivatives in (4.2.2), i.e.,

$$\frac{\partial c}{\partial x} \approx \frac{C^n_{l+1} - C^n_{l-1}}{2h}, \qquad \frac{\partial c}{\partial y} \approx \frac{C^n_{l+N} - C^n_{l-N}}{2h}.$$

Table 4.2: Indices k for the vector of unknowns U are given for elements of the vectors C_l and $\tilde{C}_m$ for a computational grid involving $N = 8$ points in the x and y directions and $M = 12$ points on the interface Γ. Labels for the five point stencil at each element k are also presented on the right-hand-side, including ghost points, denoted by $*$.

k	C_l	k	$\tilde{C}_m$
1	$C1$	20	$\tilde{C}1$
2	$C2$	22	$\tilde{C}2$
3	$C3$	24	$\tilde{C}3$
4	$C4$	26	$\tilde{C}4$
5	$C5$	32	$\tilde{C}5$
6	$C6$	33	$\tilde{C}6$
7	$C7$	34	$\tilde{C}7$
8	$C8$	35	$\tilde{C}8$
9	$C9$	42	$\tilde{C}9$
10	$C10$	43	$\tilde{C}10$
11	$C11$	44	$\tilde{C}11$
12	$C12$	45	$\tilde{C}12$
13	$C13$	52	$\tilde{C}13$
14	$C14$	54	$\tilde{C}14$
15	$C15$	56	$\tilde{C}15$
16	$C16$	58	$\tilde{C}16$
17	$C17$		
18	$C18$		
19	$C19$		
21	$C20$		
23	$C21$		
25	$C22$		
27	$C23$		
28	$C24$		
29	$C25$		
30	$C26$		

U_k	$k-N$	$k-1$	k	$k+1$	$k+N$
$C1$	$*$	$*$	1	2	9
$C2$	$*$	1	2	3	10
$C3$	$*$	2	3	4	11
$C4$	$*$	3	4	5	12
$C5$	$*$	4	5	6	13
$C6$	$*$	5	6	7	14
$C7$	$*$	6	7	8	15
$C8$	$*$	7	8	$*$	16
$C9$	1	$*$	9	10	17
$C10$	2	9	10	11	18
$C11$	3	10	11	12	19
$C12$	4	11	12	13	21
$C13$	5	12	13	14	23
$C14$	6	13	14	15	25
$C15$	7	14	15	16	27
$C16$	8	15	16	$*$	28
$C17$	9	$*$	17	18	29
$C18$	10	17	18	19	30
$C19$	11	18	19	21	31
$\tilde{C}1$	$*$	$*$	20	22	32
$C20$	12	19	21	23	$*$
$\tilde{C}2$	$*$	20	22	24	33
$C21$	13	21	23	25	$*$
$\tilde{C}3$	$*$	22	24	26	34
$C22$	14	23	25	27	36
$\tilde{C}4$	$*$	24	26	$*$	35

By substituting the normal vector $\mathbf{n}$ for each of the four sides of the square interface into (4.2.2) and rearranging, we obtain the boundary conditions on Γ,

$$\begin{aligned} D_I\frac{\partial c}{\partial y} &= D_O\frac{\partial c}{\partial y} = P(C_l^n - \tilde{C}_m^n) \quad \text{(top)}, &(4.2.6)\\ D_I\frac{\partial c}{\partial y} &= D_O\frac{\partial c}{\partial y} = -P(C_l^n - \tilde{C}_m^n) \quad \text{(bottom)}, &(4.2.7)\\ D_I\frac{\partial c}{\partial x} &= D_O\frac{\partial c}{\partial x} = P(C_l^n - \tilde{C}_m^n) \quad \text{(left), and} &(4.2.8)\\ D_I\frac{\partial c}{\partial x} &= D_O\frac{\partial c}{\partial x} = -P(C_l^n - \tilde{C}_m^n) \quad \text{(right).} &(4.2.9)\end{aligned}$$

To remove the ghost points on the interface, the equality between boundary conditions for C_l^n and $\tilde{C}_m^n$ is used. We demonstrate with an example for points on the bottom wall of the square interface (ignoring the additional boundary conditions for corner points).

Discretising (4.2.7) for points in $\mathbf{X}_O$, we have:

$$D_O\left(\frac{C_{l+N}^n - C_{l-N}^n}{2h}\right) = -P(C_l^n - \tilde{C}_m^n),$$

$$\Rightarrow C_{l+N}^n = C_{l-N}^n - 2P\frac{h}{D_O}(C_l^n - \tilde{C}_m^n). \quad (4.2.10)$$

For points in $\mathbf{X}_I$ we have:

$$D_I\left(\frac{\tilde{C}_{m+M/3}^n - \tilde{C}_{m-M/3}^n}{2h}\right) = -P(C_l^n - \tilde{C}_m^n),$$

$$\Rightarrow \tilde{C}_{m-M/3}^n = \tilde{C}_{m+M/3}^n - 2P\frac{h}{D_I}(C_l^n - \tilde{C}_m^n). \quad (4.2.11)$$

If we consider a point in $\mathbf{X}_O$ on the bottom boundary, the five point stencil used in (4.2.4) requires C_{l+N}^n, which is a ghost point. To remove C_{l+N}^n from (4.2.4), we substitute (4.2.10) into (4.2.4), giving us:

$$\begin{aligned} (1+4\xi_O)\,C_l^{n+1} + \frac{P\Delta t}{2h}C_l^{n+1} - \xi_O\left(C_{l+1}^{n+1} + C_{l-1}^{n+1} + 2C_{l-N}^{n+1}\right) - \frac{P\Delta t}{h}\tilde{C}_m^{n+1}\\ = (1-4\xi_O)\,C_l^n - \frac{P\Delta t}{2h}C_l^n + \xi_O\left(C_{l+1}^n + C_{l-1}^n + 2C_{l-N}^n\right) + \frac{P\Delta t}{h}\tilde{C}_m^n.\end{aligned}$$

We remove the remaining ghost points in our discretisation using the boundary conditions (4.2.6), (4.2.7), (4.2.8), and (4.2.9). This is where the bookkeeping becomes very complicated because we have to use the appropriate C_l^n and $\tilde{C}_m^n$ in our boundary conditions. In other words, since we wish to solve the system of $N^2 + M$ equations simultaneously, we rewrite the system of equations by replacing C_l^n and $\tilde{C}_m^n$ by elements U_k^n based on the relationships between indices l and m, and index k in the vector of unknowns, U. This process, while tedious, leads to a system of equations which we can write in matrix-vector form as

$$B_1 U^{n+1} = B_0 U^n,$$

and is block-tridiagonal. The coefficient matrices B_1 and B_0 are far too complex to present here. Given the complexity of forming these coefficient matrices for a square, constant-in-time interface, this method would be much more difficult than the IB method to set up for arbitrarily shaped, moving interfaces.

Having discretised the equations (4.2.1) and (4.2.2), we can run simulations for the finite difference (FD) and immersed boundary (IB) methods with the same parameters. We present the differences between the numerical solutions in order to provide an analysis of the strengths and weaknesses of using the IB method for simulating diffusion in cellular media.

4.2.2 Qualitative Comparison of IB and FD Method Solutions

For our two-dimensional tests, we use the following Gaussian distribution centered at (x_0, y_0) for the initial concentration taken at time $t = t_0$:

$$c(t_0, x, y) = \frac{1}{\sqrt{4\pi D t_0}} e^{-\frac{(x-x_0)^2+(y-y_0)^2}{4Dt_0}}. \qquad (4.2.12)$$

We make this choice of initial condition because, in the absence of restriction to diffusion, (4.2.12) provides the (time-dependent) function for the displacement of a molecule that was at $x = (x_0, y_0)$ at time $t = t_0$.

We first demonstrate the immersed boundary (IB) method and finite difference (FD) method results for a constant diffusion coefficient D throughout the domain. We plot contours of concentration for the IB method (left) and FD method (right) in Figure 4.6. The cellular parameters used here are $P = 1.0\,\mu\text{m/ms}$, and $D_I = D_O = 1.0\,\mu\text{m}^2/\text{ms}$ at $t = 0.425$ ms. For the computational domain, we use $N = 200$ points in the x and y directions, $M = 400$ points along the interface Γ, mesh size $\Delta x = \Delta y = 0.0275$, and a time step of $\Delta t = 5 \times 10^{-4}$.

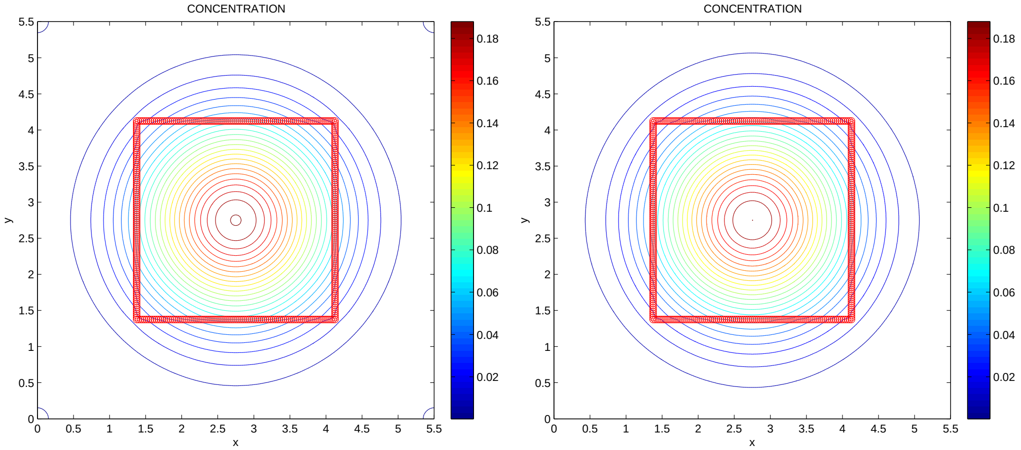

Figure 4.6: Contours of concentration for the IB method (left) and FD method (right) at $t = 0.425$ ms. The parameters used are $P = 1.0\,\mu\text{m/ms}$, and $D_I = D_O = 1.0\,\mu\text{m}^2/\text{ms}$, with $N = 200$.

Next, we demonstrate the results for more cellular-like parameters where the diffusion coefficient D_I inside the cell is not equal to the diffusion coefficient D_O outside the cell. We plot contours of concentration for the IB and FD methods in Figure 4.7, where $P = 0.01\,\mu\text{m/ms}$, $D_I = 1.56\,\mu\text{m}^2/\text{ms}$, $D_O = 2.12\,\mu\text{m}^2/\text{ms}$, $t = 0.5$ ms, and $N = 200$.

The contours of concentration demonstrate the qualitative behaviour of diffusion for the two simulations. In Figure 4.6, we see that the contours appear quite similar for both methods, meaning that for these parameter values, the IB method appears to produce valid results. In Figure 4.7, the contours appear quite similar inside the square interface, whereas they differ more outside the interface. The bottom two plots

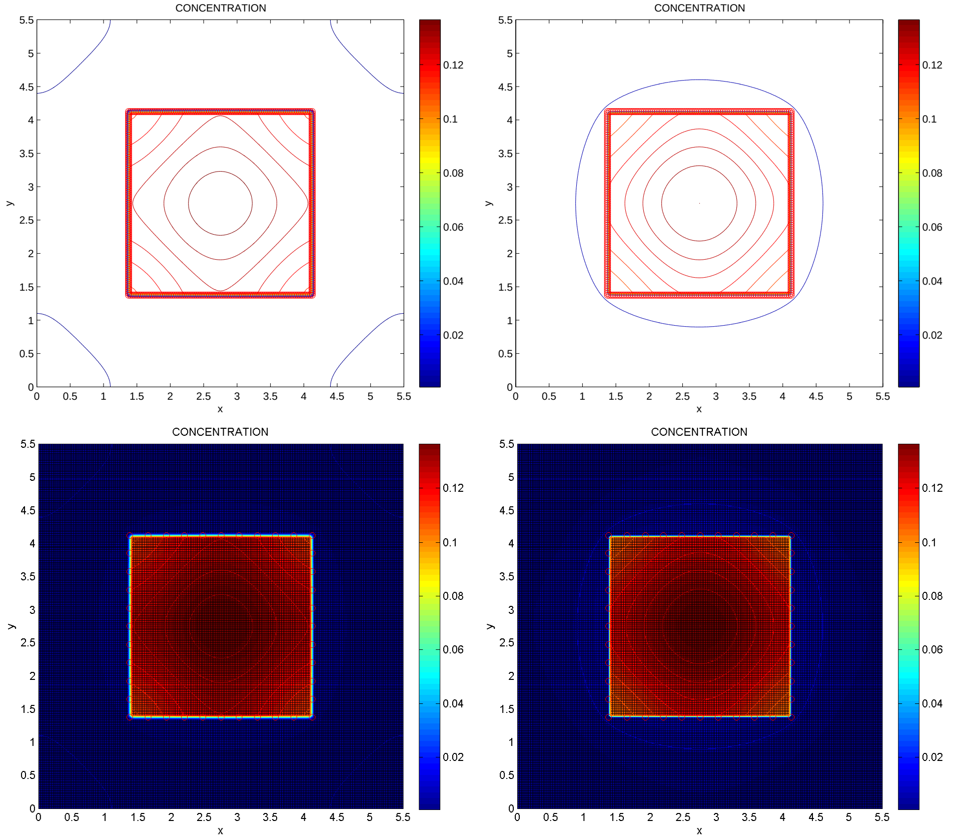

Figure 4.7: Contours of concentration for the IB method (left) and FD method (right) at $t = 0.5$ ms. The parameters used here are $P = 0.01$ μm/ms, $D_I = 1.56$ μm^2/ms, and $D_O = 2.12$ μm^2/ms. The bottom row also includes a plot of the numerical solutions, where concentration values at each point are displayed.

are a combination of the concentration values and corresponding contours. Here, the differences in concentration values between the FD and IB method simulations are less obvious, and the two simulations appear to be qualitatively the same in behaviour.

An alternate view of concentration is given in Figure 4.8 for an IB method simulation. We can clearly see the sharp drop in concentration at the four sides of the square interface.

To further investigate the differences between the FD and IB methods, we plot the relative and absolute differences in concentration between the two methods at each point in the computational mesh, with $N = 200$. In Figure 4.9, the cellular parameters are $P = 0.1$ μm/ms, $D_I = 1.0$ μm^2/ms, and $D_O = 1.0$ μm^2/ms. On the left, we plot

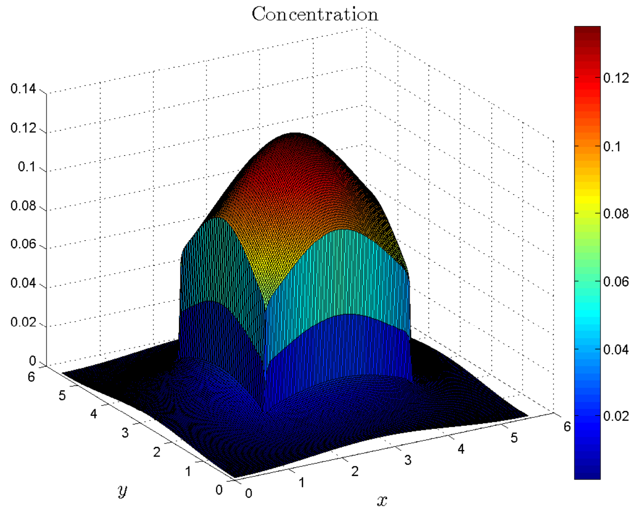

Figure 4.8: A three-dimensional view of concentration values for the IB method, where $P = 0.1$ μm/ms, $D_I = 1.56$ μm^2/ms, $D_O = 2.12$ μm^2/ms, and $t = 0.45$ ms. We can see here the sharp drop in concentration at the square interface.

the absolute difference, and on the right, we plot the relative difference. In Figure 4.10, similar graphs are produced, except that the diffusion coefficient is discontinuous, with $D_I = 1.56$ μm^2/ms and $D_O = 2.12$ μm^2/ms.

We can see from the error graphs that the differences in concentration between the two methods are quite large for $P \leq 1.0$ μm/ms, whereas the two methods agree comparatively well for $P \geq 1.0$ μm/ms. In both cases, the absolute and relative errors are largest at the interface, and outside.

One reason why the results appear worse near the interface Γ is due to the way the FD numerical solution is used at the interface. Specifically, the FD method calculates two values of concentration at each point on the interface, but only one value is used in the error calculations. This is especially problematic for small permeability P. The more impermeable a membrane is, the greater the jump in concentration will be at the interface. This means that the difference in concentration values for the FD method at each interface grid point will be greater than for large P. Correspondingly, the difference in FD and IB method solutions will be larger for small P since the IB method does not as accurately model the discontinuity in concentration at the

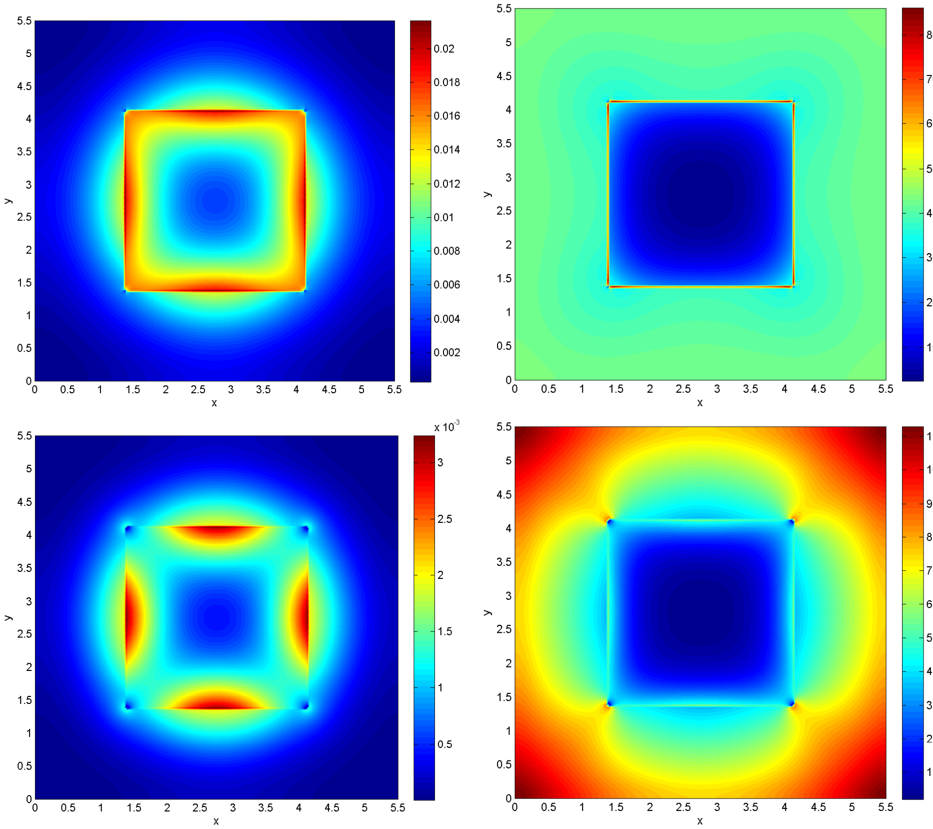

Figure 4.9: Comparison of FD and IB method simulations, where the difference in concentration values at each point is displayed. On the left, we plot the absolute difference, and on the right, we plot the relative difference (in percent). Here we consider a constant diffusion coefficient, $D_I = D_O = 1.0\ \mu\text{m}^2/\text{ms}$, $P = 0.1\ \mu\text{m/ms}$ (top row), $P = 1.0\ \mu\text{m/ms}$ (bottom row), and $t = 0.35$ ms.

interface Γ.

This small inaccuracy in the IB method at the interface will affect not only the solution at the interface, but also outside for the example problems where particles are diffusing outward from an initially large concentration at the center of the square cell. The numerical schemes proposed for the IB method are therefore less accurate currently for small P, e.g., $P \leq 1.0\ \mu\text{m/ms}$.

Another inaccuracy in the IB numerical scheme is that we approximate the discontinuity in diffusion coefficient with the average of DI and DE (interior and exterior) at the interface Γ for the IB method. This produces a smoothed concentration over the interface that will not be produced by the FD method. Therefore, this may be another contributing factor to the larger errors found near the interface Γ.

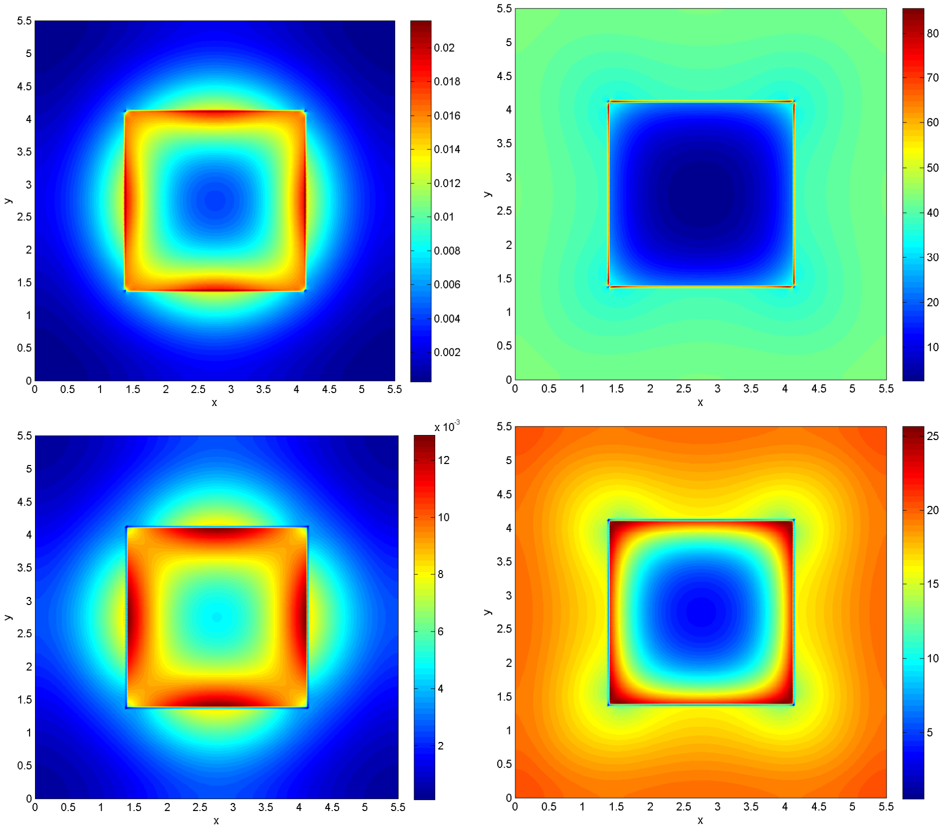

Figure 4.10: Comparison of FD and IB method simulations, where the difference in concentration values at each point is computed and displayed. On the left, we plot the absolute difference, and on the right, we plot the relative difference (in percent). The cellular parameters used here are $D_I = 1.56$ μm^2/ms, $D_O = 2.12$ μm^2/ms, $P = 0.1$ μm/ms (top row), $P = 1.0$ μm/ms (bottom row), and $t = 0.35$ ms.

Another interesting observation is that, for the initial concentration used in the above simulations, the relative error begins to increase early in the simulation, reaches a maximum, then decreases for longer time t. This is because the jump in concentration increases initially, then decreases as concentration equalizes. At this point, the IB method solutions match the FD method solutions more closely.

Overall, the IB method agrees well qualitatively with the FD method. In this sense, the numerical techniques used in the IB method are valid for simulating diffusion in cellular media with discontinuous diffusion coefficients and semipermeable membranes. Although we would like quantitatively accurate information as well, it is not realistic to ever get 100% accurate results for real systems. Therefore, we are most interested in qualitatively accurate results that can be used to validate diffusion MRI techniques for very coarse cellular configurations.

Before concluding our discussion of the IB method with some examples of irregular interfaces, we present some numerical tests for orders of convergence to further investigate the accuracy of the IB method.

4.2.3 Convergence Analysis

Having demonstrated a qualitative comparison between the IB and FD methods, we present the orders of convergence for the two methods. We again consider the square interface problem, with initial concentration given by (4.2.12), and vary the cellular parameters of diffusion coefficient D and permeability P. In Table 4.3 and 4.4, we consider a constant D, and in Table 4.5, we consider a discontinuous D.

Table 4.3: Errors and rates of convergence for the FD and IB methods, where $D_I = D_O = 1.0$ µm^2/ms, and $P = 0.10$ µm/ms.

	Finite Difference Method				Immersed Boundary Method			
	t=0.26		t=0.52		t=0.26		t=0.52	
N	$\|L_2\|$	p	$\|L_2\|$	p	$\|L_2\|$	p	$\|L_2\|$	p
25	9.2685E-04		4.0938E-04		1.5199E-03		2.4522E-03	
50	2.3347E-04	1.99	1.1318E-04	1.85	4.0799E-04	1.90	7.5307E-04	1.70
100	4.7093E-05	2.31	2.5412E-05	2.16	1.1595E-04	1.82	2.1397E-04	1.82

Table 4.4: Errors and rates of convergence for the FD and IB methods, where $D_I = D_O = 1.0$ μm^2/ms, and $P = 1.0$ μm/ms.

	Finite Difference Method				Immersed Boundary Method			
	t=0.30		t=0.51		t=0.30		t=0.51	
N	$\|L_2\|$	p	$\|L_2\|$	p	$\|L_2\|$	p	$\|L_2\|$	p
25	7.5975E-04		3.4728E-04		8.3913E-04		6.0122E-04	
50	1.9087E-04	1.99	9.0901E-05	1.93	2.3569E-04	1.83	2.3654E-04	1.35
100	3.8506E-05	2.31	1.8909E-05	2.27	6.8912E-05	1.77	9.2563E-05	1.35

Table 4.5: Errors and rates of convergence for the FD and IB methods, where $D_I = 1.56$ μm^2/ms, $D_O = 2.12$ μm^2/ms, and $P = 0.10$ μm/ms.

	Finite Difference Method				Immersed Boundary Method			
	t=0.27		t=0.45		t=0.27		t=0.45	
N	$\|L_2\|$	p	$\|L_2\|$	p	$\|L_2\|$	p	$\|L_2\|$	p
25	5.3026E-04		2.8291E-04		2.2653E-03		2.8037E-03	
50	1.3126E-04	2.01	7.7172E-05	1.87	6.8413E-04	1.73	8.4824E-04	1.72
100	2.7385E-05	2.26	1.8148E-05	2.09	2.1067E-04	1.70	2.4230E-04	1.81

We can see from the above convergence tests that the rate of convergence for the FD method is roughly second-order, and is less than second-order for the IB method. Without more accurately handling the discontinuity in concentration at the interface Γ, the IB method cannot achieve second-order convergence. An additional result is that the values of D and P do not appear to significantly affect the numerical convergence of the IB method. This suggests that the scheme converges for small P and discontinuous D, and changing these parameters will not cause the simulation to converge at slower rates.

One final result that is needed to demonstrate both the validity and flexibility of the IB method to simulate diffusion in cellular media is to consider irregular interfaces Γ, such as circles and ellipses, since square interfaces are not commonly found in cellular media, especially in brain cells. We will present plots of concentration to qualitatively describe the simulations, as well as a convergence analysis for circular interfaces.

4.3 Irregular Interfaces

To demonstrate the flexibility of the IB method for simulating diffusion in cellular media, we consider a few interface problems where Γ is circular, elliptical, and where there are a group of circles. The computational grid is the standard Cartesian grid, and the computations proceed in the same manner as with the square interface. The shape of the interface is simply represented by a group of points (shown as small red circles in the following figures). Since irregular interfaces are simple to implement, the IB method is a powerful tool for studying these kinds of configurations.

As we do not have an analytical solution, and our FD method discussed in 4.2.1 is only for square cells, we do not validate the accuracy of these results. However, there is no reason to expect the configurations presented here to be less accurate than those presented in the previous section.

Figure 4.11 presents plots of concentration for a circular interface Γ with two different sets of cellular parameters. A three-dimensional plot of concentration is presented in Figure 4.12 to better visualize the qualitative properties of the numerical solution for a circular interface. Figures 4.13 and 4.14 present four more simulations, where we vary the size, shape, and cellular parameters of the immersed interface Γ.

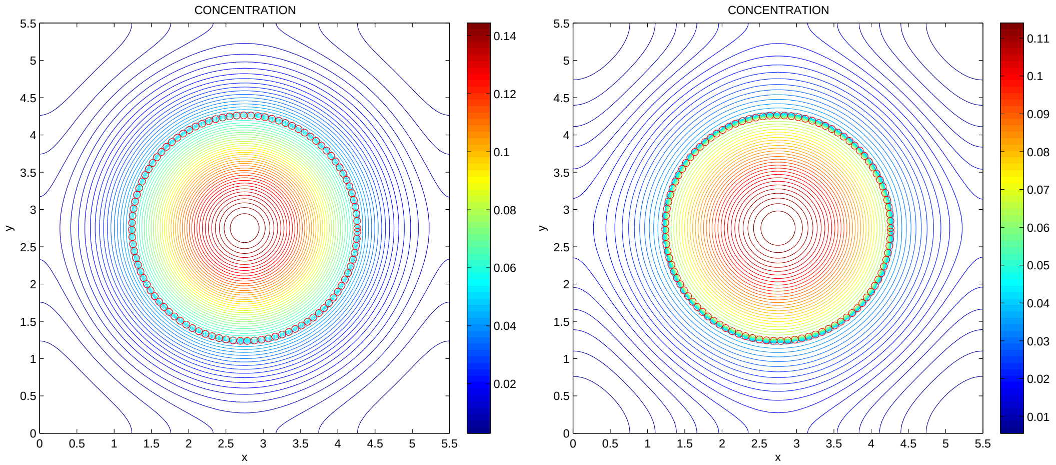

Figure 4.11: Contours of concentration for the IB method at $t = 0.5$ ms. The parameters used here are $P = 1.0\,\mu\text{m/ms}$, $D_I = D_O = 1.0\,\mu\text{m}^2/\text{ms}$ (left), and $D_I = 1.56\,\mu\text{m}^2/\text{ms}$ and $D_O = 2.12\,\mu\text{m}^2/\text{ms}$ (right).

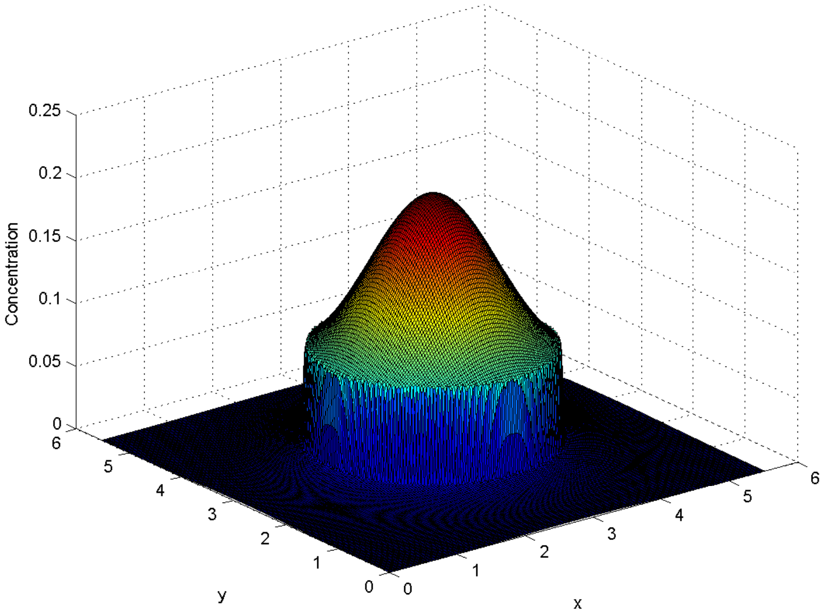

Figure 4.12: A three-dimensional view of concentration values for the IB method, where $P = 0.1$ µm/ms, $D_I = 1.56$ µm^2/ms, and $D_O = 2.12$ µm^2/ms, and $t = 0.25$ ms. We can see here the sharp drop in concentration at the interface.

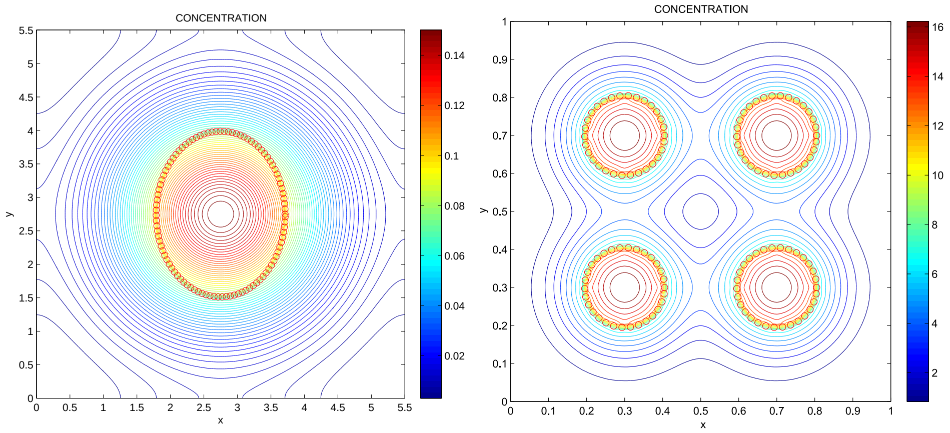

Figure 4.13: Contours of concentration for the IB method for an elliptical interface (left), and a group of four circles (right). The parameters used here are $D_I = D_O = 1.0$ µm^2/ms, $P = 1.0$ µm/ms (left), and 2.0 µm/ms (right).

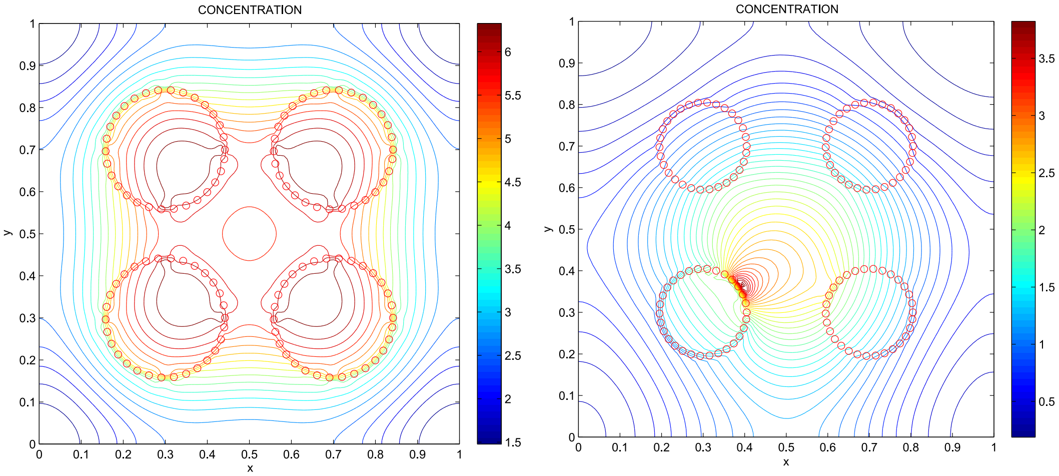

Figure 4.14: Contours of concentration for the IB method for a group of four circles. For the figure on the left, the Gaussian distribution used for the initial concentration is centered at the center of the domain, and is off-centered for the figure on the right. The cellular parameters used here are $D_I = D_O = 1.0$ µm^2/ms, and $P = 2.0$ µm/ms.

The IB method is clearly a very powerful numerical technique for simulating fluid-structure problems. As shown, this method can be applied to cellular media problems to simulate diffusion of particles, restricted by various tissue configurations. Standard methods involve body-conformal grids which can become computationally expensive, and can be avoided using the IB method approach.

We finish the discussion of the IB numerical scheme with a convergence analysis for simulations involving circular interfaces, as shown in Figure 4.11. In Table 4.6 we consider a constant D, and in Tables 4.7 and 4.8, we consider a discontinuous diffusion coefficient.

Table 4.6: Errors and rates of convergence for the IB method with a circular interface, where $D_I = D_O = 1.0$ µm^2/ms, and $P = 0.10$ µm/ms.

	t=0.135		t=0.265		t=0.450		t=0.525	
N	$\|L_2\|$	p	$\|L_2\|$	p	$\|L_2\|$	p	$\|L_2\|$	p
25	6.0807E-03		5.5800E-03		5.7885E-03		5.5940E-03	
50	9.4940E-04	2.68	2.5777E-03	1.11	3.2020E-03	0.85	3.1725E-03	0.82
100	3.7770E-04	1.33	1.2148E-03	1.09	1.4540E-03	1.14	1.4119E-03	1.17

Table 4.7: Errors and rates of convergence for the IB method with a circular interface, where $D_I = 1.56$ μm^2/ms, $D_O = 2.12$ μm^2/ms and $P = 0.10$ μm/ms.

	t=0.095		t=0.190		t=0.285		t=0.380	
N	$\lVert L_2 \rVert$	p	$\lVert L_2 \rVert$	p	$\lVert L_2 \rVert$	p	$\lVert L_2 \rVert$	p
25	2.3370E-03		5.2845E-03		6.1976E-03		6.0339E-03	
50	1.1897E-03	0.97	3.3432E-03	0.66	3.9679E-03	0.64	3.9507E-03	0.61
100	5.3300E-04	1.16	1.5768E-03	1.08	1.8423E-03	1.11	1.7992E-03	1.13

Table 4.8: Errors and rates of convergence for the IB method with a circular interface, where $D_I = 1.56$ μm^2/ms, $D_O = 2.12$ μm^2/ms, and $P = 10$ μm/ms.

	t=0.065		t=0.125		t=0.215		t=0.250	
N	$\lVert L_2 \rVert$	p	$\lVert L_2 \rVert$	p	$\lVert L_2 \rVert$	p	$\lVert L_2 \rVert$	p
25	3.5330E-03		1.3757E-03		1.0190E-03		1.0288E-03	
50	9.2720E-04	1.93	5.0250E-04	1.45	7.0040E-04	0.54	7.5750E-04	0.44
100	1.8560E-04	2.32	1.9740E-04	1.35	3.6710E-04	0.93	4.0100E-04	0.92

The above rates of convergence demonstrate that the IB method is still less than second-order for circular interfaces Γ. The convergence rates appear worse for the circular interface than for the square interface likely because the interface points do not lie on the computational grid. As shown by Leveque et al. [23], advanced techniques may be used to achieve second-order convergence when an interface cuts through the computational domain.

Overall, the IB method we have implemented appears to behave as reported in the literature, with less than second-order accuracy, and is certainly a powerful tool for simulating diffusion in cellular media.

Chapter 5

Conclusion and Future Work

Diffusion magnetic resonance imaging (MRI) is a field of great research interest with emphasis on improving the accuracy of imaging schemes, validating current methodologies, and investigating new applications. We proposed an immersed boundary (IB) method for efficiently simulating diffusion in complex media as a possible tool in testing the hypotheses of common diffusion imaging techniques, mainly the assumption of Gaussian distributions in DWI and DTI. The IB method can be applied well to diffusion in brain tissue since semipermeable membranes of various shapes may be implemented with relative ease.

To validate and test the results from the IB method, a second numerical technique was implemented using standard finite differences for a square interface. Numerical tests revealed that the IB method matched well qualitatively with the simulations using the finite difference method for permeability coefficients $P \geq 1.0$ μm/ms. Inaccuracies in the IB method implementation at the interface Γ, particularly in handling the discontinuity in diffusion coefficient and concentration across the interface, are exaggerated for small P, i.e., low permeability.

Tests for rates of convergence revealed that the IB method has less than second-order convergence for all cellular parameters considered with the square interface, and approximately first-order convergence for the irregular interfaces. The convergence results therefore demonstrate that a more complex method of handling discontinuity at the interfaces is required to achieve second-order convergence. This would ensure that the IB method can be applied with greater success for much smaller values of P and for irregular interfaces.

The IB method is known to be less accurate when applied to models involving discontinuous solutions across infinitely thin membranes. Special consideration is needed, and advanced techniques have been proposed in the literature (e.g., Leveque et al. [23]), to achieve second-order (and higher) accuracy throughout the computational domain.

To demonstrate the relative ease and efficiency of modeling diffusion with irregular interface shapes, simulations using the IB method were run with non-square interfaces. To set up such simulations using finite difference, finite element, or finite volume methods would be far more computationally expensive and difficult to implement. For this reason, we propose that the IB method is well suited to simulating diffusion in biological material.

As the IB method has not been used to our knowledge in the simulation of diffusion in connection with diffusion imaging, the results of our study are promising. For example, using the proposed IB method, one could simulate MR signals from the dephasing of hydrogen atoms (in water molecules) as is done in actual MRI experiments. From this signal, one could calculate the apparent diffusion coefficient and compare it to the known (imposed) diffusion coefficient. For simulations involving homogeneous media (e.g., no impermeable membranes), one expects agreement between the apparent diffusion coefficient and the imposed diffusion coefficient. For a heterogeneous problem, it could be seen how well the two diffusion coefficients agree. From such studies, one could test the hypotheses used in DWI and DTI that diffusion follows a Gaussian distribution (as in the free motion of water molecules).

In addition, we would like to consider other interface shapes, such as long, fiber-like interfaces, and shapes with greater irregularity. Our hope is that our IB method could be used as a tool with application to diffusion MRI, as well as simulating diffusion of contrast-enhanced dye (CED), and other clinical applications such as the development of targeted drugs.

Bibliography

[1] Cell membrane components and functions. In M.D. Binder, N. Hirokawa, and U. Windhorst, editors, *Encyclopedia of Neuroscience*, pages 596–601. Springer Berlin Heidelberg, 2009.

[2] Grey matter. In M.D. Binder, N. Hirokawa, and U. Windhorst, editors, *Encyclopedia of Neuroscience*, pages 1768–1768. Springer Berlin Heidelberg, 2009.

[3] Neuron. In M.D. Binder, N. Hirokawa, and U. Windhorst, editors, *Encyclopedia of Neuroscience*, pages 2751–2751. Springer Berlin Heidelberg, 2009.

[4] F. Aboitiz, A.B. Scheibel, R.S. Fisher, and E. Zaidel. Fiber composition of the human corpus callosum. *Brain Research*, 598:143–153, 1992.

[5] D.C. Alexander. An introduction to computational diffusion MRI: the diffusion tensor and beyond. In J. Weickert and H. Hagen, editors, *Visualization and Processing of Tensor Fields*, Mathematics and Visualization, pages 83–106. Springer Berlin Heidelberg, 2006.

[6] T. Arbogast and M.F. Wheeler. A characteristics-mixed finite element method for advection-dominated transport problems. *SIAM Journal on Numerical Analysis*, 32(2):404–424, 1995.

[7] F. Auricchio, F. Brezzi, and C. Lovadina. Mixed finite element methods. In *Encyclopedia of Computational Mechanics*, volume 1, chapter 9. 2004.

[8] R. Bammer, S. Keeling, M. Augustin, K.P. Pruessmann, R. Wolf, R. Stollberger, H.P. Hartung, and F. Fazekas. Improved diffusion-weighted single-shot echo-

planar imaging (EPI) in stroke using sensitivity encoding (SENSE). *Magnetic Resonance in Medicine*, 46:548–554, 2001.

[9] M.J. Berger and M.J. Aftosmis. Aspects (and aspect ratios) of Cartesian mesh methods. In *Proc. 16th Int. Conf. Numer. Methods Fluid Dyn.*, 1998.

[10] D. Clarke, M. Salas, and H. Hassan. Euler calculations for multi-element airfoils using Cartesian grids. *AIAA J.*, 24:1128–35, 1986.

[11] C. Dawson and R. Kirby. Solution of parabolic equations by backward Euler-mixed finite element methods on a dynamically changing mesh. *SIAM Journal on Numerical Analysis*, 37(2):424–442, 2000.

[12] M. Domin, S. Langner, N. Hosten, and L. Linsen. Direct glyph-based visualization of diffusion MR data using deformed spheres. In L. Linsen, H. Hagen, and B. Hamann, editors, *Visualization in Medicine and Life Sciences*, Mathematics and Visualization, pages 185–204. Springer Berlin Heidelberg, 2008.

[13] U. Essmann and M. Berkowitz. Dynamical properties of phospholipid bilayers from computer simulation. *Biophysical Journal*, 76(4):2081 – 2089, 1999.

[14] B. Griffith and C.S. Peskin. On the order of accuracy of the immersed boundary method: Higher order convergence rates for sufficiently smooth problems. *Journal of Computational Physics*, 208:75–105, 2005.

[15] P. Hagmann, L. Jonasson, P. Maeder, J.P. Thiran, Van J. Wedeen, and R. Meuli. Understanding diffusion MR imaging techniques: From scalar diffusion-weighted imaging to diffusion tensor imaging and beyond. *Radiographics*, 26(1):205–223, October 2006.

[16] J.P. Hollman. *Heat Transfer*. McGraw-Hill, NY, 1997.

[17] T.Y. Hou and Z. Shi. An efficient semi-implicit immersed boundary method for the Navier-Stokes equations. *Journal of Computational Physics*, 227:8968–8991, 2008.

[18] H. Huang, K. Sugiyama, and S. Takagi. An immersed boundary method for restricted diffusion with permeable interfaces. *Journal of Computational Physics*, 228:5317–5322, 2009.

[19] J. Keener and J. Sneyd. *Mathematical Physiology.* Springer-Verlag, NY, 1998.

[20] Y. Kim and C.S. Peskin. 2–D parachute simulation by the immersed boundary method. *SIAM Journal on Scientific Computing*, 28(6):2294–2312, 2006.

[21] L.L. Latour, K. Svoboda, P.P. Mitra, and C.H. Sotak. Time-dependent diffusion of water in a biological model system. *Proc. Natl. Acad. Sci. USA*, 91(4):1229–1233, 1994.

[22] A.T. Layton. Modeling water transport across elastic boundaries using an explicit jump method. *SIAM J. Sci. Comput.*, 28:2189–2207, December 2006.

[23] R.J. Leveque and Z. Li. The immersed interface method for elliptic equations with discontinuous coefficients and singular sources. *SIAM Journal on Numerical Analysis*, 31(4):1019–1044, 1994.

[24] J. Mattiello, P.J. Basser, and D. Le Bihan. The b matrix in diffusion tensor echo-planar imaging. *Magnetic Resonance in Medicine*, 37(2):292–300, 1997.

[25] R. Mittal and G. Iaccarino. Immersed boundary methods. *Annu. Rev. Fluid Mech.*, 37:239–261, 2005.

[26] K.W. Morton and D.F. Mayers. *Numerical Solutions of Parial Differential Equations: An Introduction.* Cambridge University Press, 2nd edition, 2005.

[27] D.G. Norris. The effects of microscopic tissue parameters on the diffusion weighted magnetic resonance imaging experiment. *NMR in Biomedicine*, 14:77–93, 2001.

[28] C.S. Peskin. *Flow Patterns Around Heart Valves.* PhD thesis, Albert Einstein College of Medicine, 1972.

[29] C.S. Peskin. The immersed boundary method. *Acta Numerica*, 11:479–517, 2002.

[30] R.M.A. Roque-Malherbe. Diffusion in porous materials. In *Adsorption and Diffusion in Nanoporous Materials*, chapter 5. CRC Press, March 2007.

[31] J.M. Stockie and S.I. Green. Simulating the motion of flexible pulp fibres using the immersed boundary method. *Journal of Computational Physics*, 147(1):147 – 165, 1998.

[32] A. Szafer, J. Zhong, A.W. Anderson, and J.C. Gore. Diffusion-weighted imaging in tissues: Theoretical models. *NMR in Biomedicine*, 8:289–296, 1995.

[33] J.W. Thomas. *Numerical Partial Differential Equations: Finite Difference Methods*, volume 22 of *Texts in Applied Mathematics*. Springer-Verlag, Berlin, New York, 1995.

[34] H.C. Torrey. Bloch equations with diffusion terms. *Physical Review*, 104:563–565, Nov 1956.

[35] L.B. Tran and H.S. Udaykumar. A particle-level set-based sharp interface Cartesian grid method for impact, penetration, and void collapse. *J. Comput. Phys.*, 193:469–510, January 2004.

[36] A. Tveito and R. Winther. Finite difference schemes for the heat equation. In J.E. Marsden, L. Sirovich, M. Gulubitsky, W. Jager, J.E. Marsden, L. Sirovich, M. Golubitsky, and W. Jager, editors, *Introduction to Partial Differential Equations*, volume 29 of *Texts in Applied Mathematics*, pages 117–158. Springer Berlin Heidelberg, 2005.

[37] H.S. Udaykumar, M.M. Rao, and W. Shyy. Elafint: A mixed Eulerian-Lagrangian method for fluid flows with complex and moving boundaries. *Int. J. Numer. Methods Fluids*, 22:691–705, 1996.

[38] I. Vattulainen and O.G. Mouritsen. Diffusion in membranes. In P. Heitjans and J. Karger, editors, *Diffusion in Condensed Matter*, pages 471–509. Springer Berlin Heidelberg, 2005.

[39] T. Ye, R. Mittal, H.S. Udaykumar, and W. Shyy. An accurate Cartesian grid method for viscous incompressible flows with complex immersed boundaries. *Journal of Computational Physics*, 156:209–40, 1999.

[40] D. De Zeeuw and K.G. Powell. An adaptively refined Cartesian mesh solver for the Euler equations. *Journal of Computational Physics*, 104:56–68, 1993.

[41] Y.C. Zhou, S. Zhao, M. Feig, and G.W. Wei. High order matched interface and boundary method for elliptic equations with discontinuous coefficients and singular sources. *Journal of Computational Physics*, 213:1–30, 2006.